© 2017. Published by The Company of Biologists Ltd | Journal of Cell Science (2017) 130, 2344-2358 doi:10.1242/jcs.200808

RESEARCH ARTICLE

Secreted tissue inhibitor of matrix metalloproteinase restricts *trans*-synaptic signaling to coordinate synaptogenesis

Jarrod Shilts and Kendal Broadie*

ABSTRACT

Synaptogenesis is coordinated by *trans*-synaptic signals that traverse the specialized synaptomatrix between presynaptic and postsynaptic cells. Matrix metalloproteinase (Mmp) activity sculpts this environment, balanced by secreted tissue inhibitors of Mmp (Timp). Here, we use the simplified *Drosophila melanogaster* matrix metalloproteome to test the consequences of eliminating all Timp regulatory control of Mmp activity at the neuromuscular junction (NMJ). Using *in situ* zymography, we find Timp limits Mmp activity at the NMJ terminal and shapes extracellular proteolytic dynamics surrounding individual synaptic boutons. In newly generated *timp* null mutants, NMJs exhibit architectural overelaboration with supernumerary synaptic boutons. With cell-targeted RNAi and rescue studies, we find that postsynaptic Timp limits presynaptic architecture. Functionally, *timp* null mutants exhibit compromised synaptic vesicle cycling, with activity that is lower in amplitude and fidelity. NMJ defects manifest in impaired locomotor function. Mechanistically, we find that Timp limits BMP *trans*-synaptic signaling and the downstream synapse-to-nucleus signal transduction. Pharmacologically restoring Mmp inhibition in *timp* null mutants corrects bone morphogenetic protein (BMP) signaling and synaptic properties. Genetically restoring BMP signaling in *timp* null mutants corrects NMJ structure and motor function. Thus, Timp inhibition of Mmp proteolytic activity restricts BMP *trans*-synaptic signaling to coordinate synaptogenesis.

KEY WORDS: MMP, Synaptomatrix, Neuromuscular junction, BMP, *Drosophila*

INTRODUCTION

The synaptic cleft is populated with a complex extracellular network of secreted and transmembrane proteins, yet we know little about the extracellular mechanisms that act to shape this critical cellular interface (Broadie et al., 2011; Dani and Broadie, 2012). This synaptomatrix contains integrin, heparan sulfate proteoglycan and cognate receptors for a host of known secreted and transmembrane ligands (Dani et al., 2014; Heikkinen et al., 2014; Jumbo-Lucioni et al., 2016). Extracellular proteins in the cleft are extensively remodeled in parallel with intercellular changes that accompany synaptic maturation and activity-dependent plasticity (Dityatev et al., 2010; Kurshan et al., 2014). Extracellular matrix metalloproteinase (Mmp) enzymes catalyze synaptic remodeling by proteolytically cleaving the secreted and transmembrane substrates regulating synapse structural integrity, and modulating intercellular signaling between presynaptic and postsynaptic partners (Huntley, 2012; Yasunaga et al., 2010). Given the powerful organizing effects of these proteases, their activity must be tightly regulated. One key mechanism is secretion of tissue inhibitors of Mmps (Timps), which restrict Mmp activity to proper spatial and temporal windows (Arpino et al., 2015). Whenever Mmp regulation is disrupted, developmental abnormalities and disease often result (Huntley, 2012; Malemud, 2006). Improper Mmp expression and activity is implicated in a range of neurological disorders, including schizophrenia (Lepeta and Kaczmarek, 2015), addiction (Liu et al., 2010), epilepsy (Pollock et al., 2014) and autism spectrum disorder (ASD) (Abdallah and Michel, 2013). As the most common heritable ASD and intellectual disability, Fragile X syndrome (FXS) underscores the importance of preserving Mmp balance to control proper synaptic structure and function (Reinhard et al., 2015; Siller and Broadie, 2011). Importantly, the Mmp inhibitor minocycline alleviates synaptic and behavioral phenotypes in FXS disease models (Bilousova et al., 2009; Siller and Broadie, 2011, 2012), and has shown promise in clinical trials for human patients (Leigh et al., 2013), showing that elevated Mmp activity is causally linked to FXS neuropathology (Doll and Broadie, 2014).

Since Mmp dysregulation produces pronounced synaptic defects in disease states, we hypothesized that loss of the endogenous Mmp control mediated by Timp would disrupt synapse architecture and function. We took advantage of the simplified *Drosophila melanogaster* matrix metalloproteome to test consequences of genetically ablating all Timp regulatory control over Mmp activity (Dear et al., 2016). In contrast to mammals, which have at least 24 Mmps and four partially redundant Timps (Page-McCaw et al., 2007), *Drosophila* has a single secreted Mmp (Mmp1), a single membrane-anchored Mmp (Mmp2) and a single Timp, all of which are highly conserved and can interact with their respective human homologs (Llano et al., 2000; Page-McCaw et al., 2003). In the *Drosophila* nervous system, Mmps direct both axonal targeting (Miller et al., 2008) and dendritic remodeling (Yasunaga et al., 2010). Recently, we found that Mmp1 and Mmp2 regulate *trans*-synaptic signaling at the neuromuscular junction (NMJ) to modulate synaptic structure and function (Dear et al., 2016). Moreover, we have causally linked *trans*-synaptic signaling dysregulation to synaptic defects in the *Drosophila* FXS model (Friedman et al., 2013). One *trans*-synaptic pathway important for both synaptic structure and function involves bone morphogenetic protein (BMP) signaling via the Glass Bottom Boat (Gbb) ligand (Keshishian and Kim, 2004; McCabe et al., 2003). Gbb secreted from the muscle regulates NMJ structure, whereas Gbb secreted from the motor neuron regulates neurotransmission (Berke et al., 2013; James et al., 2014). Gbb ligand in the extracellular space surrounding synaptic boutons activates downstream phosphorylated Mothers Against Decapentaplegic (pMAD) signal transduction locally at the synapse and distantly within motor neuron nuclei of the central nervous system (Smith et al., 2012; Sulkowski et al., 2014). Synaptic pMAD

Department of Biological Sciences, Kennedy Center for Research on Human Development, Vanderbilt University, Nashville, TN 37235, USA.

*Author for correspondence (kendal.broadie@vanderbilt.edu)

J.S., 0000-0002-0959-0583; K.B., 0000-0003-3783-6023

Received 19 December 2016; Accepted 29 May 2017

Journal of Cell Science

Journal of Cell Science (2017) 130, 2344-2358 doi:10.1242/jcs.200808

is associated with assembly of functional neurotransmission machinery at the NMJ, whereas the accumulation of nuclear pMAD promotes NMJ growth (Sulkowski et al., 2016). We hypothesized that the balance of Mmp proteolytic activity controlled by Timp guides *trans*-synaptic signaling pathways to modulate both NMJ synaptic structure and function.

To test this hypothesis, we generated the first ever *timp*-specific loss-of-function null alleles using CRISPR/Cas9 genome editing (Port et al., 2014; Wang et al., 2016). Generation of specific mutations was previously intractable due to a conserved nested relationship that places the *timp* gene within an intron of the important synaptic *synapsin* gene (Godenschwege et al., 2000). We have previously shown that Timp localizes in the NMJ perisynaptic space (Dear et al., 2016), where it shows a co-dependent relationship with both secreted Mmp1 and membrane-anchored Mmp2 (Page-McCaw et al., 2003; Wei et al., 2003). In the current study, we employ *in situ* zymography in living NMJs to show that Timp inhibits synaptic Mmp function and regulates the dynamics of Mmp proteolytic activity in the extracellular space surrounding synaptic boutons. We find that loss of Timp regulation removes a restraint on synaptic architecture, resulting in the overelaboration of boutons. Using transgenic RNA interference (RNAi) (Dietzl et al., 2007) and rescue, we show Timp secretion from the postsynaptic muscle is required to regulate the presynaptic motor neuron architecture. In parallel, we find Timp also controls synaptic function. By employing FM1-43 dye imaging (Gaffield and Betz, 2007), we find Timp modulates the speed and fidelity of the synaptic vesicle (SV) cycle driving synaptic neurotransmission, and impairs the coordinated muscle peristalsis output of neuromuscular activity. In testing *trans*-synaptic signaling pathways, we discover that Timp function acts to restrict BMP signaling, with *timp* null mutants showing elevated Gbb ligand levels in the extracellular space surrounding synaptic boutons and increased downstream pMAD signal transduction at both the synapse and within motor neuron nuclei. Inhibiting proteolytic activity with minocycline treatment in *timp* null mutants restores normal BMP signaling and significantly corrects NMJ properties and output motor function. Genetically restoring normal BMP signaling in *timp* null mutants corrects NMJ architecture and functional motor output, indicating that aberrant *trans*-synaptic signaling is the causal mechanism. Taken together, these results show that neuromuscular synapses require a responsive balance of Mmp activity controlled by Timp inhibition to restrict the BMP *trans*-synaptic signaling that modulates NMJ structure and function.

RESULTS

Timp constrains the pattern of Mmp proteolytic activity at NMJ synapses

A gene-specific *timp* mutation has not been previously reported in *Drosophila* or other models, owing to the conserved nested position of *timp* within the intron of the *synapsin* locus (Pohar et al., 1999), which encodes one of the most abundant components of the presynaptic terminal (Godenschwege et al., 2004). While combined *timp-synapsin* deficiencies have been generated (Godenschwege et al., 2000), the contribution of *synapsin* has confounded the study of *timp*-specific synaptic roles (Vasin et al., 2014). We resolved this impasse by precisely targeting the *timp* locus with CRISPR/Cas9 gene editing (Gratz et al., 2013). We isolated a frame-shift, complete loss-of-function allele, hereafter designated $timp^{S1}$. The mutation is a deletion at the sixth residue, and results in a nonsense transcript (Fig. S1A). We confirmed that the $timp^{S1}$ null mutants maintain normal Synapsin localization and expression by western blotting and NMJ confocal imaging (Fig. S1B,C). Homozygous $timp^{S1}$ null mutants replicate the reduced lifespan, adult infertility and structural wing phenotypes reported for *timp-synapsin* deficiencies (Godenschwege et al., 2000), showing these phenotypes are due to loss of Timp. Null $timp^{S1}$ mutants display an average adult lifespan of 5 days (Fig. S2A), male sterility and reduced female fertility, and severe wing defects of blistering, inflation and necrosis (Fig. S2B). Interestingly, the wing phenotypes are not apparent at eclosion, but become 100% penetrant within a few days post-eclosion (Fig. S2C). In the current study, we focused on Timp synaptic functions using the well-characterized *Drosophila* larval neuromuscular junction (NMJ) model. To test the proteolytic activity at *timp* null mutant synapses, we first employed *in situ* zymography to assay Mmp enzymatic cleavage of a dye-quenched (DQ) gelatin substrate (Llano et al., 2000; Siller and Broadie, 2011). In detergent-free extracellular labeling conditions, NMJs were colabeled with the anti-horseradish peroxidase (HRP) presynaptic marker. Representative confocal images and quantitative measurements are shown in Fig. 1.

Visualized proteolytic activity is conspicuously enriched at the NMJ (Fig. 1A). The extracellular perisynaptic space surrounding HRP-labeled synaptic boutons (red) shows concentrated local gelatinase activity (green), closely resembling the previously described expression patterns of Mmp1 and Mmp2 (Dear et al., 2016). Their activity levels are strongly suppressed by ubiquitous Timp over-expression (normalized *da*-Gal4/+ transgenic control 1.00±0.18; *da*-Gal4>UAS-Timp, 0.41±0.11; P=0.014), and are undetectable following incubation with the metalloproteinase-specific inhibitor 1,10-phenanthroline (Fig. 1A). In $timp^{S1}$ null NMJs, proteolytic activity is elevated compared to in the genetic background control (w^{1118}), with striking enrichment of the zymographic signal surrounding individual synaptic boutons (Fig. 1B, arrows). In high-magnification images of single boutons, DQ gelatin fluorescence colocalizes near the HRP-labeled bouton presynaptic membrane, although activity often extends more broadly, as expected for extracellular Mmp enzymes (Fig. 1C). In line with measurements across individual synaptic boutons (Fig. 1C, dashed lines), proteolytic activity is consistently elevated in $timp^{S1}$ null mutants compared to controls (Fig. 1C′). In the control animals, Mmp activity levels are normally distributed at NMJs (Fig. 1D), although different terminals within the same animal display poorly correlated activity levels (R^2=0.260), hinting at acute synapse-dependent regulatory dynamics. In $timp^{S1}$ null synapses, the overall proteolytic activity is significantly elevated compared to controls (normalized control, 1.00±0.06; $timp^{S1}$, 1.37±0.11; P=0.001; Fig. 1D, top). The synaptic activity distribution is also strongly shifted with Timp loss, from a Gaussian distribution in controls to a multimodal distribution in *timp* null mutants, with activity peaks far beyond the control maximum (Fig. 1D, bottom). These results show that Timp function limits Mmp enzymatic activity and preserves the dynamic pattern of proteolysis across the synapse.

Timp restricts synaptic growth and bouton elaboration at NMJ synapses

To test for roles of Timp regulation of Mmp proteolytic activity in synaptic processes, we next assayed NMJ structure and function. At the *Drosophila* NMJ, we recently showed that both *mmp1* and *mmp2* mutants strongly alter synaptic architectural development, displaying a mutual suppression mechanism between the secreted and membrane-bound enzymes (Dear et al., 2016). Moreover, we

Journal of Cell Science (2017) 130, 2344-2358 doi:10.1242/jcs.200808

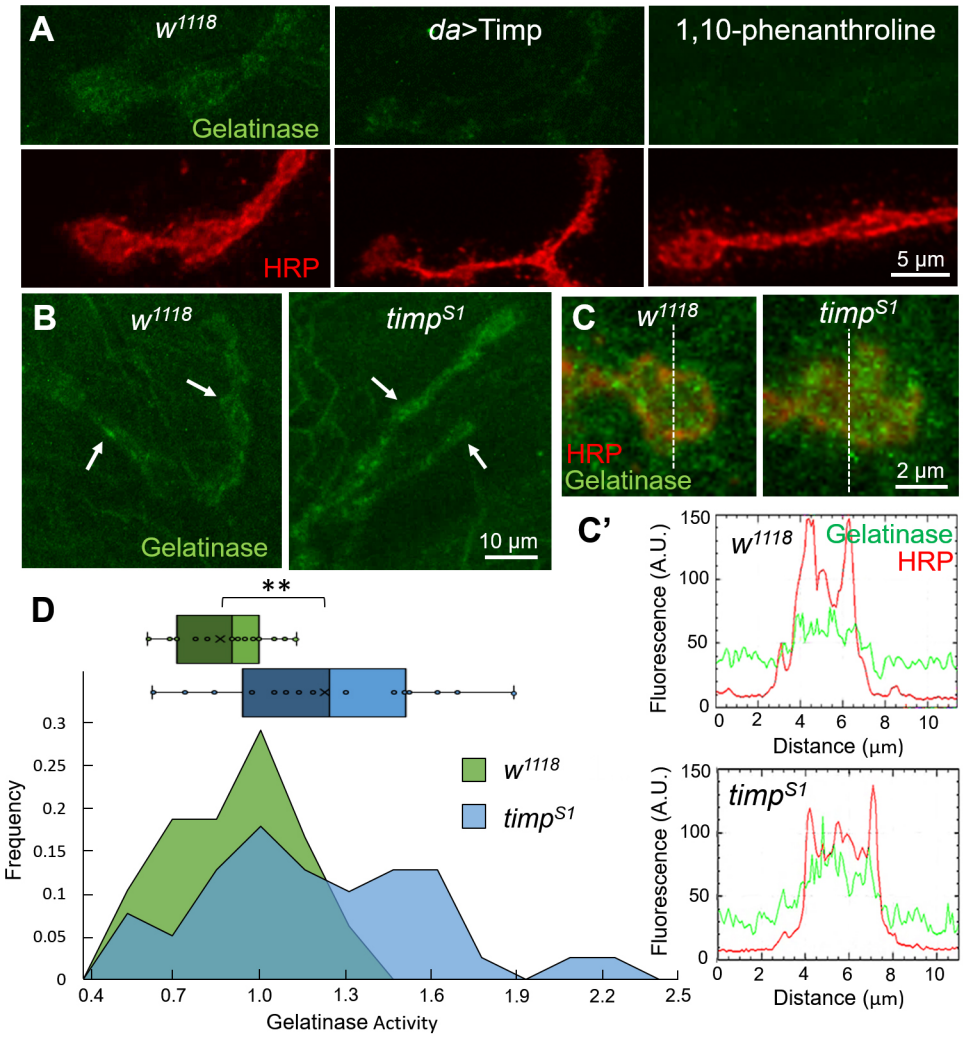

Fig. 1. Timp inhibition restricts Mmp enzymatic activity at the NMJ synapse. (A) Representative *in situ* zymography images of muscle 4 NMJ synaptic boutons in genetic background control (w^{1118}), upon Timp overexpression (*da*-Gal4>Timp) and in the control treated with Mmp inhibitor (1,10-phenanthroline). Proteolytically cleaved DQ gelatin (green, top) is shown colabeled for HRP neuronal membrane marker (red, bottom). (B) Representative *in situ* zymography gelatinase activity images comparing w^{1118} control to the *timp* null mutant ($timp^{S1}$) generated with CRISPR/Cas9. Arrows indicate proteolytic activity localized to NMJ synaptic boutons. (C) High-magnification images of single synaptic boutons in the same two genotypes. Dotted lines show location of the line-scan for gelatinase (green) and HRP (red) signals. (C′) Line-scan quantification of zymography activity (green) compared to the HRP-labeled bouton boundary (red) in w^{1118} control (top) and $timp^{S1}$ mutant (bottom). A.U., arbitrary units. (D) Quantification of NMJ gelatinase activity based on DQ gelatin fluorescence. Top, mean animal values (circles) shown as a box plot. The box represents the 25th–75th percentiles, with the median (line) and mean (×) indicated within. Whiskers extend to the minimum and maximum points excluding outlier points with values above 1.5 times the interquartile range. Bottom: gelatinase activity distribution of all NMJs assayed shown in an area plot. Sample size: $n \geq 18$ animals for each genotype, with 2–4 NMJs assayed per animal. $^{**}P<0.01$ (Welch's *t*-test).

have shown previously that pharmacologically or genetically reducing Mmp function corrects the NMJ synaptic architecture defects in the *Drosophila* FXS disease model (Siller and Broadie, 2011), with similar results reported for the mouse FXS model (Sidhu et al., 2014). Therefore, we hypothesized that Mmp regulation is a major determinant of synaptic architecture. The number of synaptic boutons, where neurotransmission occurs, is a robust measure of synaptic architecture, and is furthermore highly plastic over development and in response to activity-dependent modulation (Menon et al., 2013). At the wandering third-instar stage NMJ, each muscle shows a relatively stereotypical pattern of innervation, with similar branching arbors containing a consistent number of synaptic boutons. To test this structural parameter, we compared the genetic background control (w^{1118}) to $timp^{S1}$ null mutants, alongside experiments using a characterized transgenic UAS-*timp* RNAi line (Zhai et al., 2012) expressed with ubiquitous (*da*-Gal4), muscle-specific (*24B*-Gal4) and neuron-specific (*elav*-Gal4) drivers (Bour et al., 1995; Luo et al., 1994) versus their respective transgenic driver alone (driver/+) controls for each condition. In all eight of the genotypes (four experimental and four control), wandering third-instar muscle 4 NMJs were colabeled with the anti-HRP (red) as a presynaptic membrane marker and the anti-Discs Large (DLG, green) antibody as a postsynaptic scaffold marker. Representative images and quantitative measurements are shown in Fig. 2.

In control NMJs, muscle 4 motor termini are simple and stereotyped, with the presynaptic motor neuron innervating the muscle at a conserved location where it forms a couple of branches onto the muscle and differentiates into a series of large, evenly spaced synaptic boutons (Fig. 2A, top row). In contrast, Timp loss results in expanded arbors occupying a larger muscle surface area, with an excess of synaptic boutons (Fig. 2A, bottom row). In quantified measurements, the $timp^{S1}$ null synapses exhibit prominent over-elaboration with a significantly increased number of synaptic boutons (w^{1118} control, 11.71±0.57; $timp^{S1}$, 15.51±0.80 boutons; mean±s.e.m.), a >30% increase compared to controls (P=0.002; Fig. 2B, left). We validated these results with ubiquitous RNAi directed against Timp. Despite the knockdown level being too weak to produce null mutant viability and wing phenotypes, ubiquitous *da*-Gal4 likewise results in a smaller, but still significant, increase in synaptic bouton number (*da*-Gal4/+ control, 15.45±0.94; *da*>UAS-*timp* RNAi, 17.64±0.71 boutons; P=0.045; Fig. 2B, middle left). Cell-targeted RNAi allows tests of the source of Timp secretion that regulates synaptic bouton number. Presynaptic Timp RNAi driven by the pan-neuronal *elav*-Gal4 does not detectably alter NMJ morphology, with no significant change in the synaptic bouton number (*elav*-Gal4/+ control, 13.81±0.98; *elav*>UAS-*timp* RNAi, 15.47±0.83 boutons; P=0.155; Fig. 2B, middle right). In contrast, postsynaptic Timp RNAi driven by the muscle-specific driver *24B*-Gal4 is sufficient to fully recapitulate

Journal of Cell Science

Journal of Cell Science (2017) 130, 2344-2358 doi:10.1242/jcs.200808

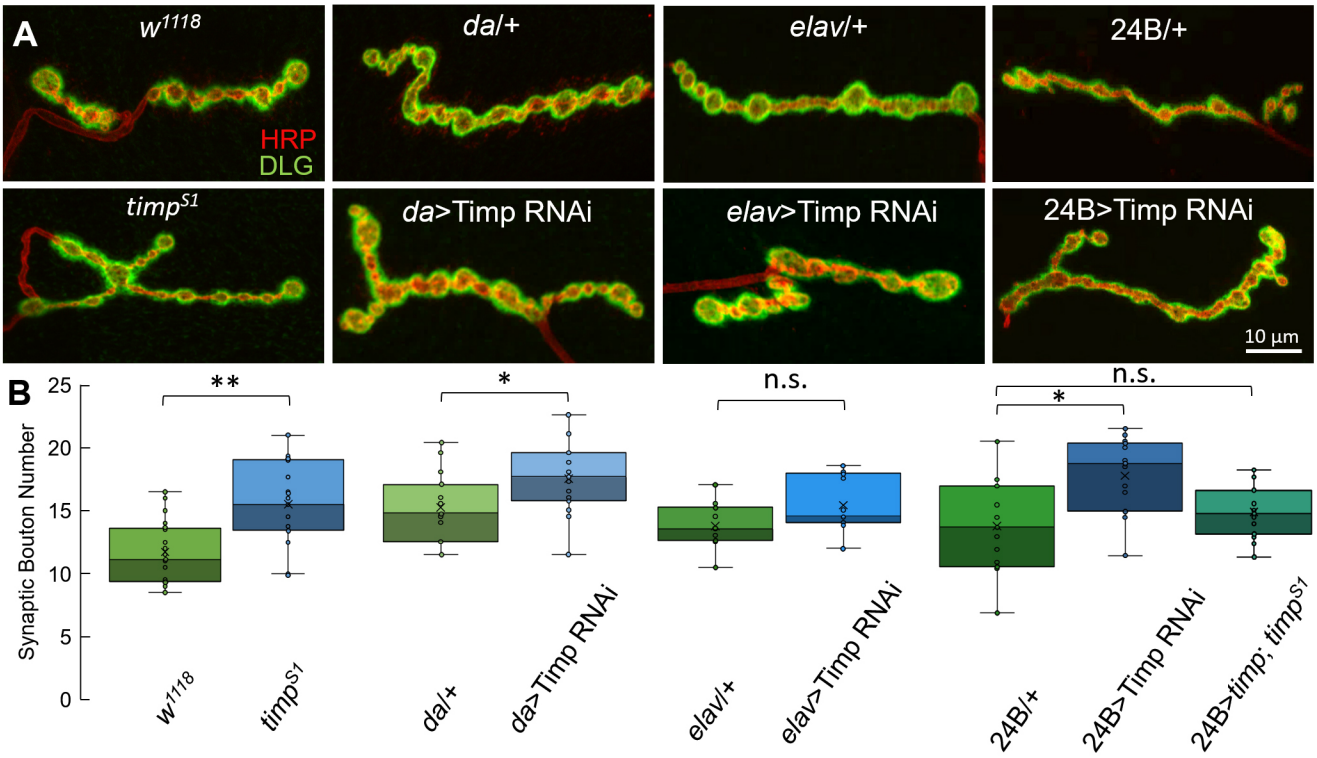

Fig. 2. Synaptic architecture overelaboration in the absence of postsynaptic Timp. (A) Representative confocal images of muscle 4 NMJ synaptic terminals in the genetic background control (w^{1118}) with the *timp* null mutant ($timp^{S1}$) below, ubiquitous Gal4 control (*da*/+) with Timp RNAi (*da*>Timp RNAi) below, presynaptic Gal4 control (*elav*/+) with Timp RNAi (*elav*>Timp RNAi) below, and postsynaptic Gal4 control (24B/+) with Timp RNAi (24B>Timp RNAi) below. All samples are colabeled for both the presynaptic HRP membrane marker (red) and the primarily postsynaptic Discs Large (DLG) scaffold (green). (B) Quantification of type Ib synaptic bouton number in the above eight paired genotypes as denoted in Fig. 1D, together with the muscle 24B>UAS-*timp* rescue in the $timp^{S1}$ null mutant. Sample size: $n \geq 8$ animals for each genotype, with $n \geq 2$ NMJs assayed per animal (total $n \geq 16$ per genotype). *$P<0.05$; **$P<0.01$; n.s., not significant (Welch's *t*-test).

the synaptic structural overelaboration (*24B*-Gal4/+ control, 13.22±1.38; *24B*>UAS-*timp* RNAi, 17.29±0.99 boutons), again showing a >30% increase compared to control ($P=0.011$; Fig. 2B, far right). To validate these findings, we drove a UAS-*timp* wild-type transgene in the $timp^{S1}$ null background with the muscle-specific *24B*-Gal4. Restoring postsynaptic Timp corrected synaptic morphology in *timp* null mutants (*24B*-Gal4/+ control, 13.22±1.38; *24B*>UAS-*timp*; $timp^{S1}$, 14.88±0.50 boutons; $P=0.373$; Fig. 2B, far right). In addition to supporting the postsynaptic secretion of *timp*, this transgenic rescue further validates the specificity of the $timp^{S1}$ allele. These results indicate that postsynaptically secreted Timp acts to constrain presynaptic motor neuron size and limit architectural elaboration of the NMJ synapse.

Timp facilitates synaptic vesicle cycling rate and functional fidelity

Synaptic structure and function are established by separate but parallel pathways (Collins and DiAntonio, 2007; Miller et al., 2012), which may be governed independently depending on the mechanistic intersection with extracellular Timp–Mmp regulation. At the *Drosophila* NMJ, we recently showed that both *mmp1* and *mmp2* mutants independently alter neurotransmission strength (Dear et al., 2016). To test Timp roles in synaptic function, we assayed the functional neurotransmission machinery at the single-bouton level in order to avoid the confounding effects of *timp* mutation on synaptic bouton number. We used the depolarization-dependent lipophilic FM1-43 dye labeling technique to monitor the synaptic vesicle (SV) cycle, including both SV endocytosis and exocytosis (Betz and Bewick, 1992). Upon depolarization with high K^+ saline (90 mM), FM1-43 dye is incorporated into vesicles ('loading') during endocytosis, providing a measure of the functional SV cycling pool size (Staples and Broadie, 2013; Vijayakrishnan et al., 2009). A second high K^+ saline depolarization in the absence of the FM1-43 dye drives vesicle fusion ('unloading') during neurotransmission exocytosis, as a measure of SV release efficacy from presynaptic boutons. We compared the genetic background control (w^{1118}) to the *timp* null mutant ($timp^{S1}$) at the muscle 4 NMJ. Representative images and quantitative measurements are shown in Fig. 3.

In control NMJs, muscle 4 motor termini robustly load FM1-43 dye upon acute depolarization, with all synaptic boutons strongly loaded and a consistent level of dye incorporation between boutons (Fig. 3A, top left). In contrast, Timp loss results in an overall decrease in FM1-43 loading, with less dye incorporated per synaptic bouton and greatly increased loading variability between boutons of the same $timp^{S1}$ terminal (Fig. 3A, bottom left). However, both genotypes appear to release dye upon repeat depolarization to reach similar unloaded endpoints (Fig. 3A, right). In quantified measurements, *timp* null mutants display significantly impaired SV endocytosis, loading less fluorescent dye across the entire NMJ (normalized w^{1118} control, 1.00±0.08; $timp^{S1}$, 0.74±0.08; mean± s.e.m., $P=0.024$; Fig. 3B, left). Inducing a second phase of depolarization to trigger FM1-43 dye exocytosis causes similar post-release levels in *timp* mutants and controls (normalized w^{1118} control, 0.45±0.05; $timp^{S1}$, 0.43±0.06; Fig. 3B, right). However, owing to the reduced loading, the percentage of FM1-43 dye released from the *timp* null synapses is decreased compared to

Journal of Cell Science

Journal of Cell Science (2017) 130, 2344-2358 doi:10.1242/jcs.200808

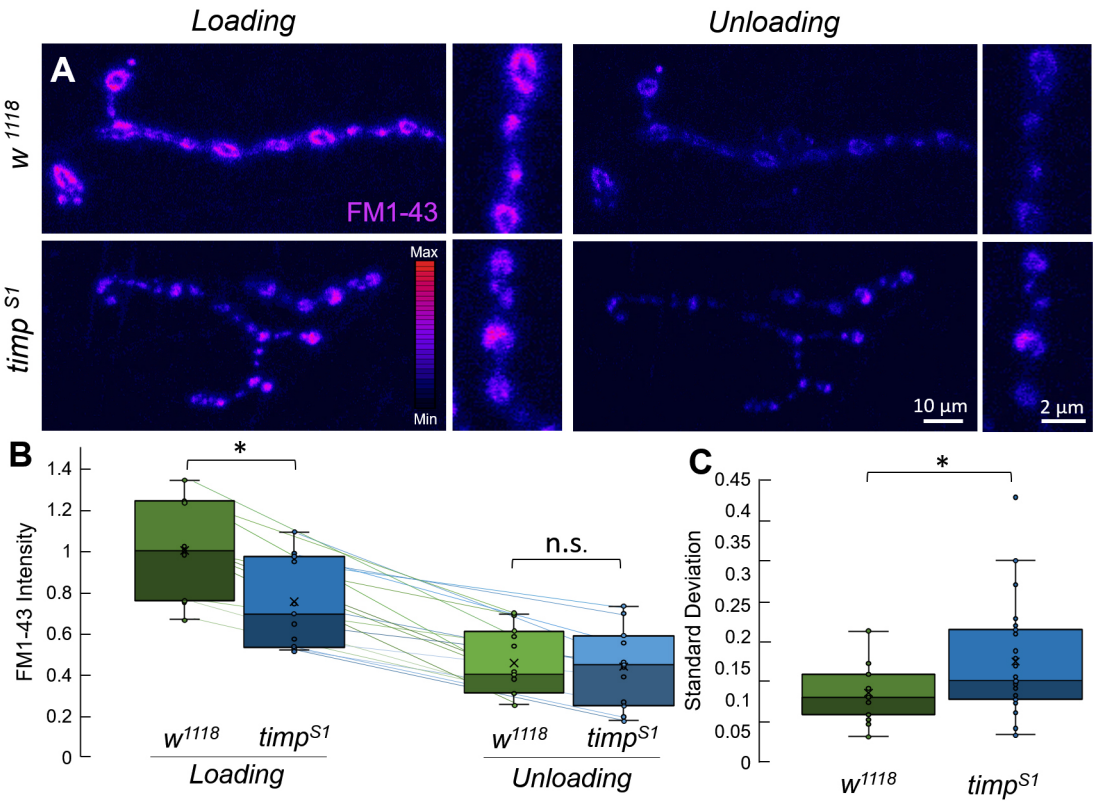

Fig. 3. Impaired SV endocytosis and SV cycle fidelity in the absence of Timp. (A) Representative confocal images of muscle 4 NMJ boutons in the genetic background control (w^{1118}, top) and *timp* null mutant ($timp^{S1}$, bottom) loaded with FM1-43 dye (purple, left) and unloaded in the absence of dye (right). For each condition, both low (left) and high (right) magnification images are shown. FM1-43 intensity is shown as a heat-map with indicated scale (lower left). (B) Quantification of synaptic vesicle dye loading and unloading intensity in the above genotypes. Lines connect points from the same NMJ, in the loaded and unloaded conditions. Sample size: $n\geq10$ animals for each genotype, with 2 NMJs assayed per animal (total $n\geq20$ for each genotype). (C) Quantification of the variation in FM1-43 dye loading between synaptic boutons within the same NMJ in the above genotypes. Sample size: $n\geq9$ NMJs per genotype and $n\geq7$ boutons per NMJ. Box plots are presented as in Fig. 1D. *P<0.05; n.s., not significant (Welch's t-test).

matched controls (w^{1118} control, 53.86±4.45; $timp^{S1}$, 42.57±5.13; Fig. 3B, lines). Together with this overall dye cycling defect, loss of Timp also causes increased cycling variability between boutons within the same NMJ terminal (Fig. 3A). Calculating the standard deviation between different dye-loaded NMJ synaptic terminals, we find that variability is significantly increased in the $timp^{S1}$ null condition compared to the controls (w^{1118} control, 0.11±0.01; $timp^{S1}$, 0.16±0.02; mean±s.e.m., P=0.038; Fig. 3C). These results show that there is impaired synaptic vesicle cycling and loss of functional fidelity in the absence of Timp, suggesting broader neurotransmission deficits.

Timp facilitates coordinated muscle peristalsis during locomotion

The decreased dye flux through the synaptic vesicle cycle led us to predict that motor function would be impaired by loss of Timp synaptic metalloproteinase regulation. To test this hypothesis, we next assayed simple larval peristaltic locomotor behavior mediated by the same neuromuscular synapses examined in all the above cellular studies (Pulver et al., 2009, 2015). We measured freely moving *Drosophila* larvae during the linear phase of locomotion on a homogeneous agarose substrate (Berni et al., 2012). In *Drosophila* larvae, locomotion proceeds via a coordinated peristaltic wave of muscle contractions proceeding along the entire length of the animal (Fig. 4A). We analyzed muscle contraction waves traveling in the posterior-to-anterior direction (arrows), from the tail to the head. In wandering third-instar larvae, we measured the duration of this segmentally coordinated motor pattern, comparing genetic background control (w^{1118}) to the *timp* null mutant ($timp^{S1}$). We also quantified the temporal latency required for the muscle peristaltic waves to propagate between the segments, which is well established to correlate with NMJ neurotransmission strength (Diaper et al., 2013). Representative still image frames taken from locomotion videos and quantitative measurements are shown in Fig. 4.

In control animals, peristaltic contraction waves proceed in a rapid and relatively invariant segmental sequence along the entire length of the larva to drive quick forwards movement (Fig. 4A, top). In sharp contrast, Timp loss results in visibly slower and delayed peristaltic waves, which take far longer to travel along the animal and result in slower locomotion (Fig. 4A, bottom). Comparing between muscle contraction events, the genetic background w^{1118} controls generate consistent wave patterns with very little temporal variation, whereas $timp^{S1}$ null mutants display a loss of contraction fidelity and a clear increase in variability. For locomotion (Fig. S3A), this defect corresponds with a trend towards decreased distance traveled per unit time (Fig. S3B). Mutant animals also exhibit changed patterns of behavior including significantly decreased exploratory turning behavior (Fig. S3C). To avoid this confounding factor, we used peristalsis measurements at high temporal resolution as a more reliable and NMJ-dependent metric for motor function comparisons. In quantified measurements, control muscle peristalsis contraction

Journal of Cell Science

Journal of Cell Science (2017) 130, 2344-2358 doi:10.1242/jcs.200808

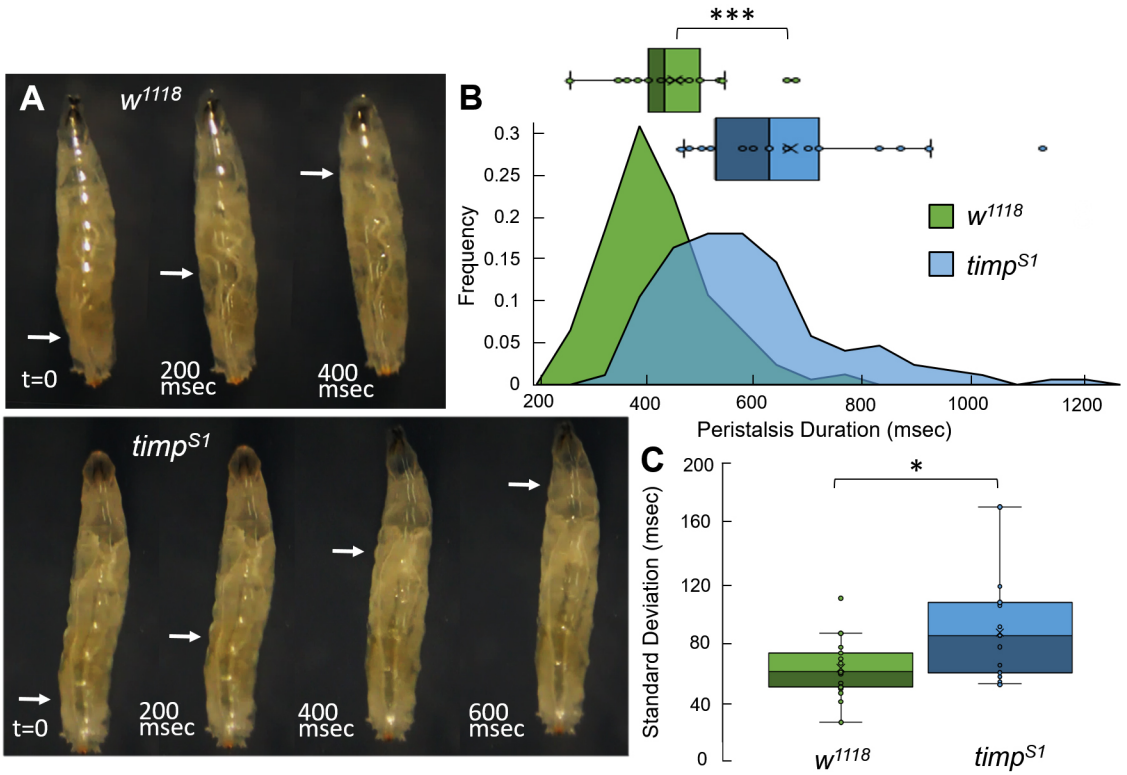

Fig. 4. Impaired peristaltic muscle contraction function in the absence of Timp. (A) Frames of movies showing larval peristaltic muscle contraction waves in the genetic background control (w^{1118}, top) and *timp* null mutant ($timp^{S1}$, bottom). Frames are spaced at 200 ms intervals from initiation to termination of the peristaltic wave. Arrows indicate the position of the wave at each interval. (B) Quantification of peristalsis wave duration. Top, times shown as a box plot, with mean animal values shown (circles). Bottom, the distribution of individual peristaltic waves shown as an area plot. (C) Quantification of the mean standard deviation for the same genotypes. Sample size: $n \geq 19$ animals for each genotype, with $n \geq 168$ peristaltic waves measured per animal for each genotype. Box plots are presented as in Fig. 1D. *$P<0.05$; ***$P<0.001$ (Welch's *t*-test).

waves conform to a narrow temporal distribution, as expected for this tightly controlled locomotor program (Fig. 4B). In contrast, *timp* null mutants display significantly delayed wave propagation. Quantified comparisons of muscle peristalsis duration in *timp* mutants show a highly significant delay (w^{1118} control 405.8±20.5; $timp^{S1}$ 539.2±26.5 ms; mean±s.e.m.), with a ∼33% protraction compared to controls ($P<0.001$; Fig. 4B, top). Comparisons between the double *timp, synapsin* deficiency and the *synapsin*-specific mutant (syn^{97}) replicate the significantly increased peristalsis duration (*timp, syn* 591.6±23.1 ms; syn^{97} 471.9±13.1; $P<0.001$; Fig. S3D), confirming the defect is due to Timp loss, although muscle expression of a *timp* transgene in a mutant background is not sufficient to rescue the phenotype. Consistent with defects at the NMJ level, the distribution of *timp* null peristaltic propagation times is substantially broader than those in matched controls, with highly variable muscle contraction rates in the absence of Timp (Fig. 4B, bottom). The variability in muscle contraction times is significantly greater in *timp* null mutants (w^{1118}, 52.2±12.5; $timp^{S1}$ 99.8±19.8 ms), with a ∼90% increase compared to controls ($P=0.006$; Fig. 4C). These results suggest that the reduced and irregular NMJ function in *timp* null mutants results in activity that is lower in amplitude and fidelity.

Timp restricts BMP *trans*-synaptic signaling at synapses and in nuclei

To identify molecular mechanisms linking local Timp dysregulation of Mmp activity to NMJ defects driving muscle peristalsis impairments, we pursued candidate pathways with known function that fit the above phenotypes. Intercellular *trans*-synaptic signaling acts as a core modulator of NMJ structure, function and motor output, including regulation of bouton number, synaptic vesicle cycling and coordinated muscle motor function (Jumbo-Lucioni et al., 2016; Parkinson et al., 2016; Wu et al., 2010). Furthermore, our recent studies have revealed highly aberrant *trans*-synaptic signaling in *mmp1* and *mmp2* mutants (Dear et al., 2016), and within the Mmp-dependent FXS disease model (Friedman et al., 2013). In particular, the BMP ligand Gbb gates synapse growth and neurotransmission strength in response to closely regulated contextual cues (Piccioli and Littleton, 2014). Within the canonical pathway, secreted Gbb ligand drives the phosphorylation of MAD (pMAD) locally within the NMJ terminal, which then relays a signal for pMAD to enter distant motor neuron nuclei in the ventral nerve cord (VNC) (McCabe et al., 2003; Smith et al., 2012). We first tested extracellular Gbb ligand levels in the NMJ synaptomatrix of the genetic background control (w^{1118}) and *timp* null mutant ($timp^{S1}$), then tested pMAD levels locally at the synapse and distally in the motor neuron nuclei. Representative images and quantitative measurements are shown in Fig. 5.

In detergent-free extracellular labeling studies, control synaptic boutons (red) are surrounded by a halo of secreted Gbb ligand (blue; Fig. 5A). In *timp* null mutants, Gbb levels are consistently elevated at NMJ terminals (Fig. 5A, right). In quantified measurements, Gbb accumulates at significantly higher levels in the perisynaptic space surrounding boutons in mutants compared to controls (normalized w^{1118} control, 1.00±0.15; $timp^{S1}$, 1.77±0.13; $P=0.008$; Fig. 5A′). If this excess Gbb ligand activates signal transduction as expected, it

Journal of Cell Science

Journal of Cell Science (2017) 130, 2344-2358 doi:10.1242/jcs.200808

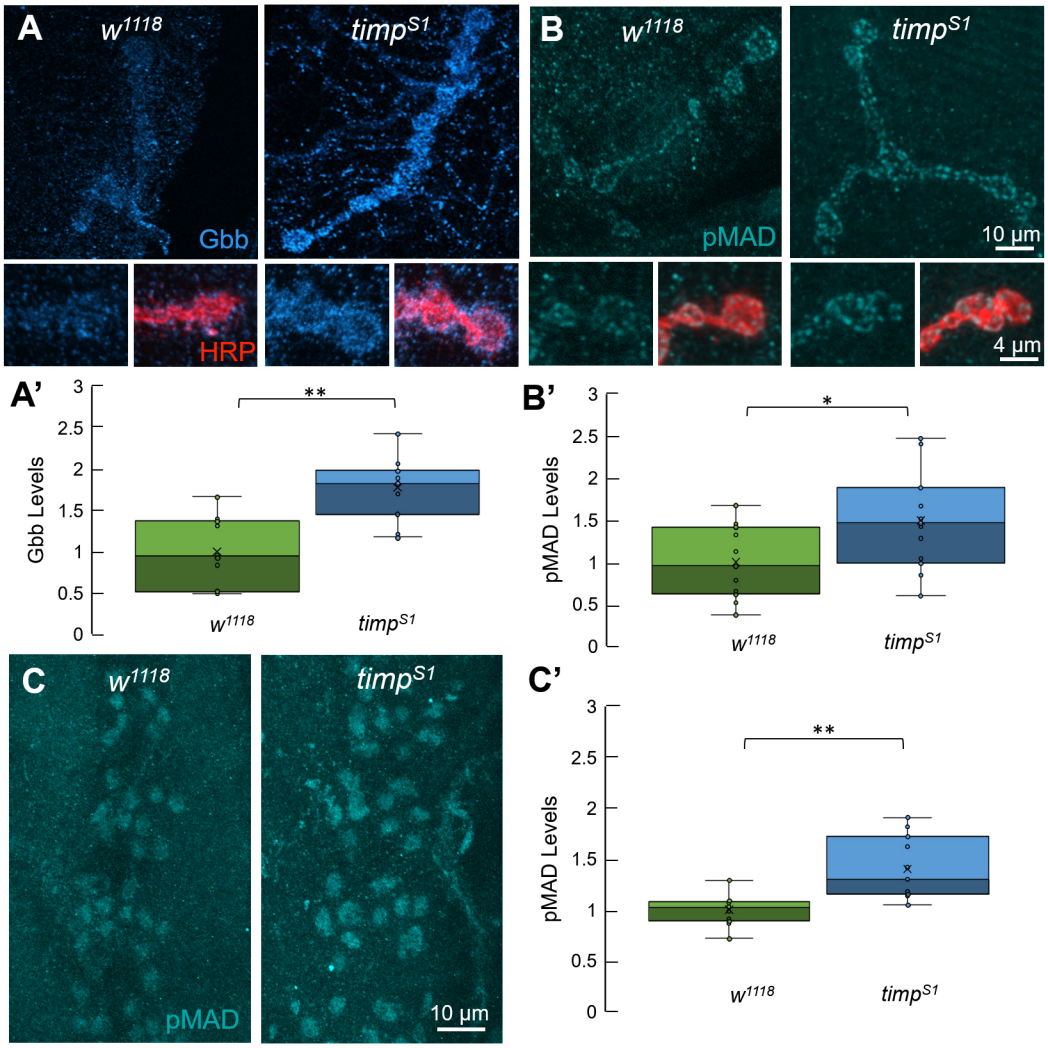

Fig. 5. BMP *trans*-synaptic signaling is suppressed by Timp function. (A) Representative confocal images of muscle 4 synaptic boutons in the genetic background control (w^{1118}, left) and *timp* null mutant ($timp^{S1}$, right) labeled for extracellular glass bottom boat (Gbb, blue). Below, high magnification NMJ bouton images colabeled for Gbb (blue) and the marker HRP (red). (A′) Quantification of extracellular Gbb ligand levels shown. (B) Representative confocal images of muscle 4 synaptic boutons labeling for phosphorylated MAD (pMAD, cyan). Below, high-magnification bouton images colabeled for pMAD (cyan) and HRP (red). (B′) Quantification of pMAD levels at the NMJ. (C) Representative confocal images of ventral nerve cord (VNC) dorsal midline motor neuron soma labeled for pMAD (cyan) in the above genotypes. (C′) Quantification of pMAD accumulation in the motor neuron nuclei. $n \geq 10$ animals per genotype. Box plots are presented as in Fig. 1D. *P<0.05; **P<0.01 (Welch's *t*-test).

will drive excess pMAD production at the terminal. Upon intracellular (detergent) labeling, control synaptic boutons (red) contain numerous pMAD puncta (cyan; Fig. 5B). In *timp* null mutants, synaptic pMAD levels are clearly elevated compared to matched controls (Fig. 5B, right). In quantified measurements, pMAD intensity within HRP-marked NMJ synaptic boutons is significantly elevated in mutants compared to controls (normalized w^{1118} control, 1.00±0.14; $timp^{S1}$, 1.61±0.20; P=0.026; Fig. 5B′). Motor neuron soma lie along the VNC dorsal midline, with nuclei selectively enriched for pMAD (Fig. 5C). Compared to genetic controls, *timp* null mutants display consistently elevated pMAD in motor neuron nuclei (Fig. 5C, right). Activated pMAD drives transcriptional changes underlying synaptic bouton formation and functional strengthening, supporting Timp roles at the synapse. In quantified measurements, pMAD intensity within motor neuron nuclei is significantly increased in the absence of Timp (normalized w^{1118} control, 1.00±0.03; $timp^{S1}$, 1.39±0.09; P<0.001; mean±s.e.m.; Fig. 5C′). These studies show that Timp restricts Gbb levels to limit both local and nuclear pMAD signal transduction that modulates NMJ structure and function.

Pharmacologically restoring Mmp inhibition corrects *timp* null mutant defects

BMP signaling misregulation in *timp* null mutants could either be a product of the demonstrated proteolytic hyperactivity occurring in the absence of inhibition by Timp (Fig. 1), or the result of an Mmp-independent Timp function (Stetler-Stevenson, 2008). To distinguish between these two possibilities, we pharmacologically restored Mmp inhibition in *timp* null mutants by using minocycline drug treatments (Golub et al., 1991). Minocycline has been well-characterized as acting via an Mmp-inhibitory mechanism, remediating FXS synaptic defects at the *Drosophila* NMJ (Siller and Broadie, 2011), as well as in the mouse disease model (Bilousova et al., 2009). To test dose-dependent correction of mutant phenotypes, we reared *timp* null mutants on a range of minocycline concentrations (20 µM to 1000 µM in food). Wild-type larvae raised

Journal of Cell Science

Journal of Cell Science (2017) 130, 2344-2358 doi:10.1242/jcs.200808

on high minocycline levels phenocopy *mmp* null mutants (Dear et al., 2016), including cellular defects and early lethality, consistent with strong Mmp inhibition. We therefore did not include animals reared in >100 µM minocycline in these analyses. We used low (20 µM) and high (100 µM) minocycline concentration to compare genetic background controls (w^{1118}) to the *timp* null mutants ($timp^{S1}$). No effects occur in synaptic bouton number (Fig. S4A) or peristaltic motor behavior (Fig. S4B) when minocycline at the high dose (100 µM) is administered to control animals. Using *in situ* zymography, we confirmed minocycline treatment can restore NMJ proteolytic activity levels in *timp* null mutants (normalized w^{1118} control, 1.00±0.05; $timp^{S1}$, 0.91±0.05; P=0.225; mean±s.e.m.; Fig. S4C,D). After treating *timp* nulls with minocycline, we assayed a wide range of phenotypes including BMP signaling, NMJ architecture and peristaltic motor function. Representative images and quantitative measurements are shown in Fig. 6.

If Mmp hyperactivity is causally linked to elevated BMP signaling (Fig. 5), then minocycline treatment should restore more normal levels of pMAD signal transduction. As the most downstream transduction output, we assayed pMAD accumulation in the VNC motor neuron nuclei as a consequence of BMP pathway activation (Fig. 6A). The pattern of nuclear pMAD levels in genetic controls and *timp* null mutants in this independent experiment closely replicates the above results. The $timp^{S1}$ mutants show clearly elevated pMAD accumulation in motor neuron nuclei along the VNC dorsal midline (Fig. 6A). In sharp contrast, *timp* mutants reared on food containing 100 µM minocycline display nuclear pMAD indistinguishable from control levels (Fig. 6A, right). In quantified measurements, pMAD levels within motor neuron nuclei are restored from the highly significant increase in the untreated mutant condition (normalized w^{1118} control, 1.00±0.07; $timp^{S1}$, 1.65±0.19; mean±s.e.m.; P=0.007), to a significantly reduced level with treatment (100 µM minocycline, 1.35±0.17), which is no longer statistically different from the genetic background control (P=0.131; Fig. 6A′). These results show that elevated Mmp activity in the *timp* null causes elevated BMP *trans*-synaptic signaling. Given that pharmacologically restoring Mmp inhibition in mutants corrects the signaling defect, we next asked whether the neuromuscular structural and functional phenotypes characterizing *timp* mutants are corrected in parallel.

Mmp inhibition by minocycline treatment is sufficient to restore *timp* null NMJ architecture (Fig. 6B). Compared to genetic controls, *timp* mutants have overelaborated NMJs with more synaptic boutons (w^{1118} control, 12.88±0.69; $timp^{S1}$, 16.32±0.95; P=0.015), whereas mutants treated with minocycline display a dose-dependent return to control architecture (20 µM: 14.25±0.60; 100 µM: 13.54±0.80 boutons). The higher dose results in bouton numbers that are indistinguishable from control, with no significant difference remaining (P=0.9; Fig. 6B′). Dose-dependent rescue is also evident in restoring motor function (Fig. 6C). Minocycline treatment is effective in reversing the mutant defects in peristaltic muscle wave propagation, shifting latencies from the broad and elevated distribution of untreated *timp* mutants (w^{1118} control, 375.5 ±14.2; $timp^{S1}$, 577.3±44.64 ms; P=0.001) in a dose-dependent return towards the faster, higher fidelity function of controls (20 µM: 504.6±9.5; 100 µM: 481.1±17.5 ms; Fig. 6D). We also calculated the variability of muscle peristalsis time to gauge effects of minocycline treatment. Inhibiting Mmp function drives a dose-dependent restoration of consistent neuromuscular control (20 µM, 56.8±5.3; 100 µM, 39.1±2.8 ms), with a dose of 100 µM minocycline leading to variability being significantly reduced from untreated mutants ($timp^{S1}$, 61.5±6.2 ms; P=0.013; Fig. 6C). At 100 µM minocycline, the mutant variability is no longer significantly different from controls (w^{1118} control, 45.9±3.7 ms; P=0.742). These results show BMP signaling, NMJ properties and motor function output are all responsive to Mmp inhibition, demonstrating that Timp regulates all these phenotypic levels via control of Mmp proteolytic activity.

Genetically restoring BMP signaling corrects *timp* null mutant defects

After demonstrating that Mmp activity upregulation causes *timp* null defects in *trans*-synaptic signaling, NMJ structure and motor function, we hypothesized that elevated BMP signaling through Gbb is the mechanism underlying synaptic and movement defects in the absence of Timp. To test this hypothesis, we corrected *trans*-synaptic signaling by genetically reducing Gbb expression in the *timp* null background with the removal of one *gbb* gene copy ($gbb^{2/+}$; $timp^{S1}$) (Nahm et al., 2010). We then repeated assays for NMJ structure and peristaltic function to measure the effects on mutant defects across these two phenotypic classes (Fig. 7). In contrast to the synaptic overgrowth in the *timp* null alone, reducing *gbb* gene dosage by 50% completely restores NMJ architecture (Fig. 7A). Quantification of synaptic bouton number again shows a significant increase in the *timp* null mutant condition alone (w^{1118} control, 13.91±0.38; $timp^{S1}$, 15.80±0.49 boutons; mean±s.e.m.; P=0.047; Fig. 7A′), whereas *timp* mutants with Gbb correction no longer display any supernumerary synaptic boutons ($timp^{S1}$ 15.80±0.49; $gbb^{2/+}$; $timp^{S1}$ 13.84±0.73 boutons; P=0.038; Fig. 7A′). Importantly, the Gbb-corrected *timp* null mutants are no longer distinguishable from controls (P=0.900; Fig. 7A′). We have shown previously that removing a single *gbb* copy alone does not affect NMJ morphology (Nahm et al., 2010), indicating a specific interaction between *gbb* and *timp*.

At a functional level, correcting BMP *trans*-synaptic signaling in *timp* null mutants also mitigates the motor peristalsis defects (Fig. 7B). Removing one copy of *gbb* strongly accelerates the aberrantly prolonged muscle contraction waves that characterize the *timp* mutant alone ($timp^{S1}$, 535.3±78.3; $gbb^{2/+}$; $timp^{S1}$, 456.7± 8.4 ms) in a highly significant improvement (P=0.001; Fig. 7B′). The gbb^{2} heterozygote alone has no effect on locomotion (w^{1118} control, 391.5±15.0; $gbb^{2/+}$, 408.1±10.4 ms; P=0.371), indicating that our intervention is specific to the Timp pathway. However, in this case, the correction in function is only partial, with a significant impairment remaining in comparison to that in the genetic background control (w^{1118}, 391.5±15.0; $gbb^{2/+}$;$timp^{S1}$, 456.7±8.4 ms; Fig. 7B′). The increase in variability between peristaltic waves in *timp* nulls (w^{1118} control, 33.8±1.7; $timp^{S1}$, 46.9±2.1 ms; P=0.022; Fig. 7B) also tends to be reduced toward higher fidelity control levels when Gbb levels are corrected, although not significantly ($gbb^{2/+}$; $timp^{S1}$, 40.8±2.2 ms; P=0.326). The ability to significantly correct both neuromuscular synapse structure and the functional motor defects of *timp* null mutants by counteracting the increase in Gbb *trans*-synaptic signaling indicates that aberrant BMP signaling causally mediates the neurological phenotypes resulting from a loss of Timp.

DISCUSSION

Remodeling of the synaptic extracellular environment is a highly dynamic process, demanding precise spatiotemporal control in response to specific developmental and activity-dependent signals (Broadie et al., 2011; Dansie and Ethell, 2011; Dityatev and Schachner, 2003; Tsilibary et al., 2014). Mmp proteolytic activity is an ideal node of regulation for the necessary responsive kinetics and

Journal of Cell Science (2017) 130, 2344-2358 doi:10.1242/jcs.200808

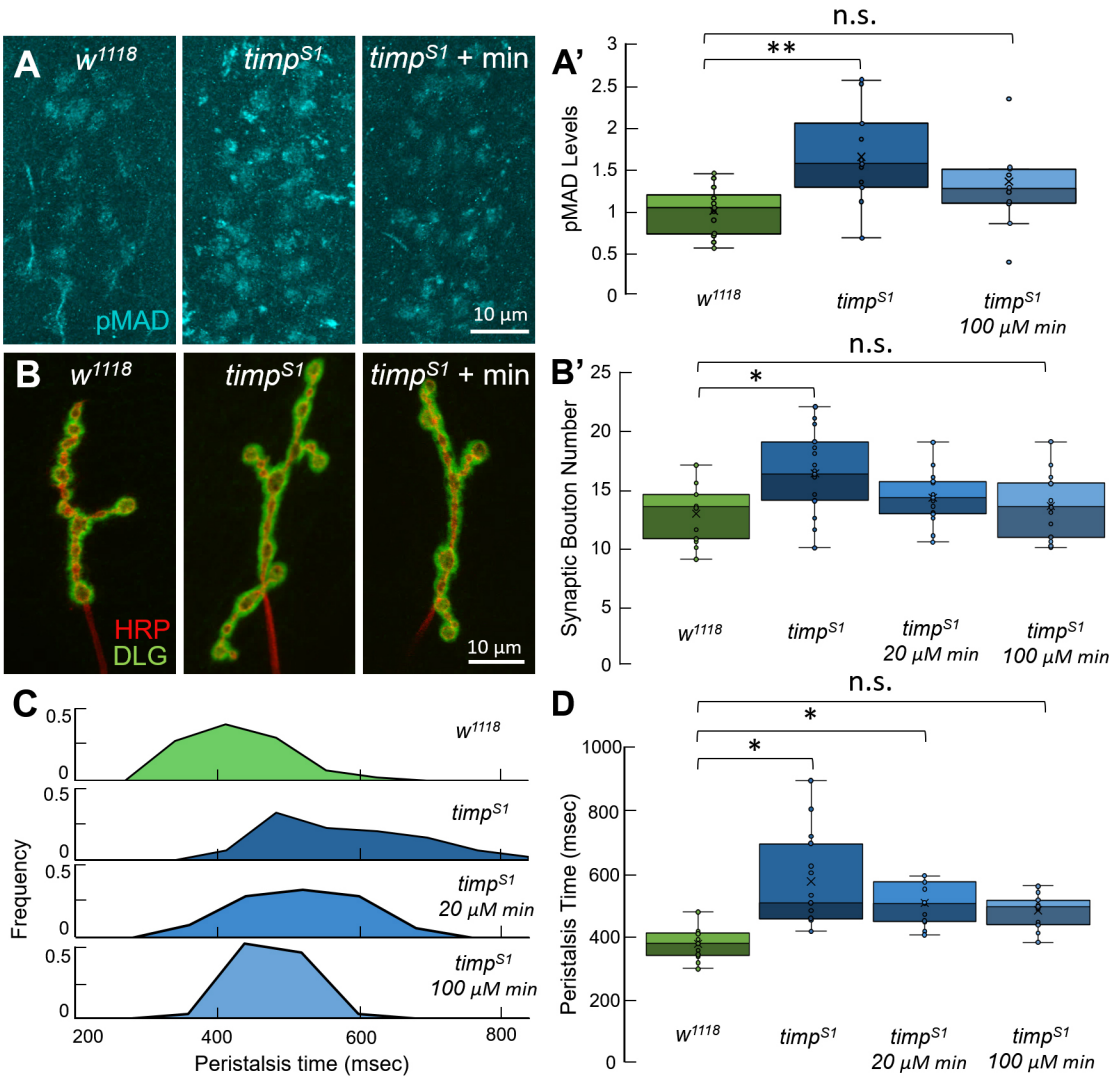

Fig. 6. Mmp inhibition rescues BMP signaling, NMJ structure and motor function. (A) Representative confocal images of ventral nerve cord (VNC) nuclei labeled for pMAD (cyan) in the genetic background control (w^{1118}), *timp* null ($timp^{S1}$) and *timp* null mutants reared with 100 µM minocycline (min). (A′) Right, quantification of pMAD levels in the motor neuron nuclei. $n \geq 10$ animals per condition. (B) Representative confocal images of muscle 4 NMJs colabeled for presynaptic HRP (red) and postsynaptic DLG (green). (B′) Right, quantification of synaptic bouton number. $n \geq 12$ animals, with two NMJs assayed per animal. (C,D) Quantification of motor function peristalsis time, with (C) the distribution of individual peristaltic waves per condition shown in area plots, and (D) the averaged times shown in box plots. $n \geq 10$ animals for each condition. *P<0.05; **P<0.01; n.s., not significant (one-way ANOVA followed by Tukey-Kramer post-hoc *t*-test). Box plots are presented as in Fig. 1D.

specificity, with Timps controlling the timing, duration and spatial specificity of enzyme function (Yamamoto et al., 2015). Taking advantage of the simplified matrix metalloproteome of *Drosophila*, with only a single functionally conserved Timp (Wei et al., 2003), we were able to eliminate all Timp function with one mutation. Using site-directed CRISPR/Cas9, we generated the first *timp* null allele, with targeted mutation of the *timp* gene, without disrupting the *synapsin* gene in which it is nested (Godenschwege et al., 2000; Pohar et al., 1999). Although nested genetic placement does not imply a functional relationship (Lee and Chang, 2013), the highly conserved nesting of *timp* in *synapsin* occurs across vertebrates and invertebrates, which are separated by hundreds of millions of years of evolution. The evolutionary conservation of timp nesting in synapsin is interesting, since synapsin encodes a key synaptic regulator (Michels et al., 2005; Vasin et al., 2014) and there is evidence of co-regulation of genes nested with Timps (Jaworski et al., 2007). In addition to *timp* loss-of-function mutants, to our knowledge no viable Mmp gain-of-function has yet been reported in *Drosophila* (Page-McCaw et al., 2003). Thus, our new CRISPR-induced *timp* null is a tool to characterize total Timp function as well as generally elevated Mmp activity as seen in the nervous system. Currently, there are relatively few reports concerning Timp loss in the nervous system (Crocker et al., 2004; Rivera et al., 2010). In mice, TIMP-2 knockout causes motor deficits (Jaworski et al., 2006) and expanded NMJ branching (Lluri et al., 2006), and TIMP-1 overexpression reduces outgrowth in cortical cells (Ould-yahoui et al., 2009), supporting findings here. In *Drosophila*, Timp overexpression inhibits NMJ growth (Dear et al., 2016), which again complements our findings.

In this study, we uncover key roles for Timp in controlling synaptic Mmp activity, thereby regulating NMJ structure, function and output. We find muscle-secreted Timp limits synaptic Mmp

Journal of Cell Science

Journal of Cell Science (2017) 130, 2344-2358 doi:10.1242/jcs.200808

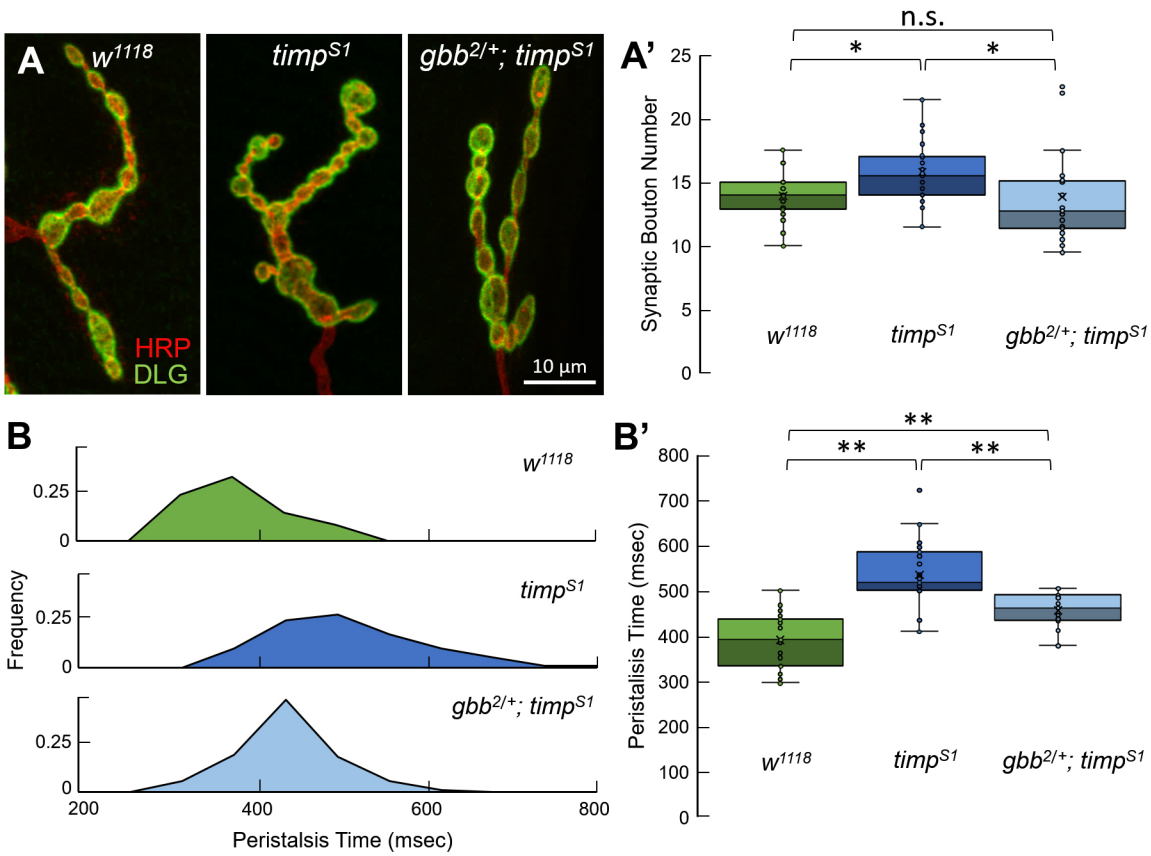

Fig. 7. Genetically correcting BMP signaling suppresses *timp* mutant defects. (A) Representative confocal images of the muscle 4 NMJ in the genetic background control (w^{1118}), *timp* null mutant ($timp^{S1}$), and *timp* null mutant with one copy of *gbb* removed ($gbb^{2/+}; timp^{S1}$). Synaptic boutons colabeled for presynaptic HRP (red) and postsynaptic DLG (green). (A′) Quantification of type Ib synaptic bouton number per NMJ terminal. $n \geq 22$ animals per genotype. (B) Distribution of all peristaltic waves measured for each genotype, showing the overall variance. (B′) Quantification of mean motor peristalsis times for every larva assayed. $n \geq 16$ animals per genotype. *$P<0.05$; **$P<0.01$; n.s., not significant (one-way ANOVA followed by Tukey-Kramer post hoc *t*-test). Box plots are presented as in Fig. 1D.

proteolytic activity and shapes the distribution of Mmp activity within the synaptomatrix (Fig. 1). This local regulation of Mmp functional dynamics has not been reported to our knowledge in neuronal synapses, but is consistent with known roles of Timp in non-neuronal contexts (Kessenbrock et al., 2010; Mittal et al., 2016). We find that postsynaptic Timp limits presynaptic NMJ architecture and bouton formation (Fig. 2). This is surprising given that individual Mmp knockdown similarly limits synaptic structure in flies and mice (Dear et al., 2016; VanSaun et al., 2003), but may suggest that both loss and gain of Mmp function converge phenotypically or that, collectively, Timp repression of multiple Mmp activities acts as a brake on synaptic growth. We find Timp also regulates synaptic function, by facilitating SV endocytosis and maintaining SV cycle fidelity (Fig. 3). In comparison, *mmp* mutants elevate transmission strength, also by altered SV cycling dynamics (Dear et al., 2016; Szklarczyk et al., 2007), consistent with Timp repression of Mmp function. We find Timp enables faster and higher fidelity muscle contraction peristalsis, driving coordinated locomotion (Fig. 4). Motor defects have consistently been found across a range of Mmp manipulations (Brkic et al., 2015; Dansie et al., 2013; Jaworski et al., 2006; Sidhu et al., 2014), although molecular mechanisms had not been identified. Taken together, these results complete our characterization of the entire *Drosophila* matrix metalloproteome in controlling neuromuscular synapse structure and function (Dear et al., 2016). The *timp* null synaptic phenotypes prompt a re-assessment: Mmps are not simply negative regulators of synaptic differentiation, but can promote structural development within a context-dependent mechanism (Dziembowska and Wlodarczyk, 2012). This work shows Timp and Mmps interact to sculpt synapse form and function.

We find that Timp limits BMP *trans*-synaptic signals mediating communication between the muscle and motor neuron, with Timp loss elevating Gbb ligand levels (Fig. 5). BMP ligands are well known to be sequestered by extracellular molecules (Larraín et al., 2000; Sengle et al., 2008), and proteolytic cleavage of these extracellular antagonists controls the distributions of signaling activity in multiple cellular contexts (Larraín et al., 2001; Schleede and Blair, 2015). In *Drosophila* neurons, Mmp2 regulates motor axon pathfinding and fasciculation (Miller et al., 2008) via Mmp2-mediated proteolytic cleavage of the ECM Fibrillin/Fibulin-related Faulty Attraction (Frac) protein to enable BMP signaling (Miller et al., 2011). Similarly, we find here elevated BMP *trans*-synaptic signaling in *timp* mutants with Mmp proteolytic hyperactivity (Fig. 5). Gbb secretion from the postsynaptic muscle regulates NMJ architecture, whereas Gbb released from the presynaptic motor neuron regulates neurotransmission function (James and Broihier, 2011; James et al., 2014). These roles are consistent with the misregulation of synaptic structure (Fig. 2) and SV cycle function (Fig. 3), respectively, seen in *timp* mutants with elevated Gbb signaling. The accumulation of Gbb in the perisynaptic synaptomatrix of *timp* null mutants drives downstream activation of pMAD signal transduction in both motor neuron synaptic

Journal of Cell Science

Journal of Cell Science (2017) 130, 2344-2358 doi:10.1242/jcs.200808

terminals and motor neuron nuclei (Fig. 5). This is consistent with pMAD activation of transcriptional programs for coordinating synapse structural and functional differentiation (Ball et al., 2010; Kim and Marqués, 2012). Gbb secreted from the postsynaptic muscle (James and Broihier, 2011) is regulated by Timp that is also secreted from the muscle (Fig. 2), which provides control for motor neuron terminals to expand in response to muscle growth and activity-dependent plasticity (Marqués and Zhang, 2006; McCabe et al., 2003). In contrast, Mmps come from both presynaptic and postsynaptic cells (Dear et al., 2016). Thus, directional Timp control acts as a specific muscle-derived mechanism to regulate Gbb *trans*-synaptic signaling.

Elevated BMP Gbb signaling in a *Drosophila* model of Troyer syndrome, a hereditary spastic paraplegia (HSP) disease, causes strikingly similar NMJ synaptic structural and functional defects to those seen upon loss of Timp (Nahm et al., 2013). Like the *timp* null mutants (Figs 2 and 3), *spartin* mutants that are causatively associated with Troyer syndrome exhibit expanded synaptic arbors and decreased FM1-43 dye SV endocytic loading with impaired motor function. Importantly, Fragile X Mental Retardation Protein (FMRP) is a downstream effector of Spartin function, limiting BMP Gbb signaling (Nahm et al., 2013). Loss of FMRP causes Fragile X syndrome (FXS), and reducing non-canonical BMP signaling alleviates the synaptic defects in *Drosophila* and mouse FXS disease models (Kashima et al., 2016). Likewise, targeted mutation of the FXS-related S6 kinase (S6K) similarly results in both expanded synaptic architecture and decreased SV endocytosis at the *Drosophila* NMJ (Zhao et al., 2015), once again resembling *timp* null phenotypes (Figs 2 and 3). As in *timp* mutants, there are also clear precedents for mutations of other key regulatory proteins increasing NMJ functional variability to compromise motor output function (Renger et al., 2000; Ueda et al., 2008). Our findings with *timp* demonstrate the utility of variability as a metric to uncover regulatory nodes that preserve the functional resiliency of the nervous system.

By pharmacologically correcting *timp* null phenotypes with the characterized Mmp inhibitor minocycline (Dziembowska et al., 2013; Siller and Broadie, 2012), we show that mutant defects are causally linked to Mmp hyperactivity (Fig. 6). Alleviation of *timp* null phenotypes is robust, albeit partial, which may reflect experimental limitations of the drug administration, or possibly reveal other Mmp-independent Timp functions (Moore and Crocker, 2012). In particular, behavioral assays of motor function show conspicuous, albeit partial, rescue (Fig. 6), which may be evidence of an Mmp-independent contribution to motor function or, more likely, that the precise spatiotemporal dynamics of Timp at the NMJ are necessary for proper motor function (Fig. 1). In rats, transient proteolytic activity in the synaptomatrix accompanies long-term potentiation and dendrite maturation (Magnowska et al., 2016), which corroborates our model that Timp dynamically restricts synaptic modulation through localized ECM proteolysis. Crucially, pharmacologically balancing Mmp activity in *timp* null mutants with minocycline treatment restores BMP *trans*-synaptic signaling (Fig. 6), and genetically correcting BMP signaling prevent synaptic and movement defects (Fig. 7). These findings support the model that Mmp activity in the synaptomatrix, under regulation by Timp, limits BMP *trans*-synaptic signals, thereby controlling NMJ synaptogenesis and functional motor output.

These studies provide an avenue for possible therapeutic treatments in a range of neurological disease states with elevated Mmp activity (Hadler-Olsen et al., 2011; Reinhard et al., 2015). In particular, Mmp hyperactivity has been causally implicated in FXS and related ASD conditions (Abdallah and Michel, 2013; Dziembowska et al., 2013; Sidhu et al., 2014; Siller and Broadie, 2011). The synaptic cytoarchitectural phenotypes of *timp* mutants phenocopy the *Drosophila* FXS model (Zhang et al., 2001), and *trans*-synaptic signaling defects are causative in synaptic structural and functional defects in this disease model (Friedman et al., 2013), including BMP signaling (Kashima et al., 2016). By re-creating the elevated Mmp activity characterizing neurological disease conditions such as FXS, our *timp* genetic tools provide insights into fundamental synaptic mechanisms with direct clinical relevance. In future studies, we plan to combine *timp* manipulations with our established *Drosophila* disease models in order to more fully dissect contributions of Mmp-dependent *trans*-synaptic signaling impairments in different neurological disease states.

MATERIALS AND METHODS

Drosophila genetics

All *Drosophila* stocks were reared on standard cornmeal, molasses and agar food in a cycling incubator with 12 h of light at 25°C and 12 h of dark at 18°C. The genetic background control for all studies was w^{1118}. RNAi knockdown studies were performed with the characterized UAS-*timp-RNAi*^{KK108268} line (Zhai et al., 2012) and compared to the isogenic control *y,* w^{1118}*; P{attP,y*$^{+}$*,w*^{3}*}*, both obtained from the Vienna *Drosophila* Resource Center (VDRC). Timp overexpression was performed using the characterized wild-type UAS-*timp* (Page-McCaw et al., 2003). The transgenic expression was driven by three drivers; ubiquitous *da*-Gal4, body muscle *24B*-Gal4 and neuronal *elav*-Gal4 lines (Bour et al., 1995; Luo et al., 1994). Genetic interaction studies between *gbb* and *timp* were performed with the characterized gbb^{2} null allele (Wharton et al., 1999). For transgenic rescue experiments, *24B*-Gal4 was recombined with the $timp^{S1}$ null allele, and placed with UAS-*timp* in the $timp^{S1}$ background. Null *timp* mutants were isolated, confirmed and maintained in a TM6 balanced stock, as described below.

Timp mutagenesis

Null *timp* alleles were generated by CRISPR/Cas9-induced non-homologous end-joining as previously described (Gratz et al., 2013). Oligonucleotides encoding a guide RNA sequence direct targeting the first *timp* exon (5′-CTTCGTGCGTCTGTGGGTGAGA-3′) were assembled into a pU6-BbsI-chiRNA vector (Addgene #45946; Gratz et al., 2013). Purified constructs were injected at 250 ng/µl into w^{1118}, *vas-Cas9 Drosophila* embryos (BestGene, Inc.). Animals reared from the injected embryos were individually crossed into a homogenized genetic background balanced over TM6. All isolated mutant alleles were screened by direct PCR sequencing to characterize the molecular lesions in the new *timp* mutants. The characterized frame-shift null allele $timp^{S1}$ was used in all phenotypic studies.

Survival and wing assays

For survival assays, newly eclosed adults were separated into vials of five animals each. Vials were kept in a 12-h-light–12-h-dark (25°C in light and 18°C in dark) cycling incubator and monitored daily. Every day at the midpoint of the light cycle, the number of live freely moving animals in each vial was counted, and the state of wings scored. Wings were categorized based on black necrosis (necrotic), blistering or inflation (blistered), notching or other deviations from normal wing shape (misshaped), or the absence of any abnormalities (normal). Since these categories are not mutually exclusive, if more than one phenotype was present then the most severe phenotype was used for categorization. Similarly, if both wings were not equivalent, the more severe wing was used.

Western blotting

Analyses were performed as previously described (Dear et al., 2016). Briefly, heads of two male and two female adults at 1 day post-eclosion were homogenized in buffer [67 mM NaCl, 2 M urea, 1.3% SDS, 1 mM EDTA, Protease inhibitor tablet (Roche), 67 mM Tris-HCl pH 8]. Samples were heated at 60°C for 10 min in NuPAGE LDS buffer (Invitrogen) and 5% 2-mercaptoethanol before loading onto 4–12% gradient Bis-Tris gels

Journal of Cell Science

(Invitrogen). Protein concentration was measured by determining the absorbance at 280 nm on a Nanodrop 2000c instrument (Thermo Scientific) to ensure equivalent loading. After electrophoresis, samples were transferred onto nitrocellulose membrane, and blocked with 5% milk in TBS-T (10 mM Tris, 150 mM NaCl, 0.05% Tween-20) for 1 h at room temperature. Samples were incubated in mouse anti-Synapsin antibody (1:2000; DSHB, 3C11) overnight at 4°C. Membranes were subsequently washed with TBS-T, incubated in goat anti-mouse-IgG secondary antibody conjugated to DyLight 800 (1:10,000; Rockland) for 2 h at room temperature, and then washed a final time in TBS-T. Blots were imaged with a Odyssey CLx infrared scanner (Licor).

Immunocytochemistry

Wandering third-instar immunolabeling was performed as previously described (Staples and Broadie, 2013). Staged animals were dissected in physiological solution (128 mM NaCl, 2 mM KCl, 4 mM $MgCl_2$, 0.2 mM $CaCl_2$, 70 mM sucrose, 5.5 mM trehalose, 5 mM HEPES, pH 7.2) and fixed in 4% paraformaldehyde for 15 min. Preparations were then (1) permeabilized with 0.2% Triton X-100 (for HRP, DLG, Synapsin and pMAD staining) or (2) processed without detergent for extracellular labeling (Gbb). Primary antibodies used were: goat anti-HRP conjugated to Cy3 (1:200; Jackson Laboratories 123-165-021) or Alexa Fluor 647 (123-605-021), mouse anti-DLG [1:200; Developmental Studies Hybridoma Bank (DSHB), 4F3], mouse anti-Synapsin (1:200; DSHB, 3C11), rabbit anti-Gbb (1:100; Dani et al., 2012) and rabbit anti-pMAD (1:1000; Persson et al., 1998) antibodies. Primary antibodies were incubated overnight at 4°C. Secondary antibodies used were: goat anti-mouse-IgG conjugated to Alexa Fluor 488 or Alexa Fluor 568, goat anti-rabbit-IgG conjugated to Alexa Fluor 488, and goat anti-guinea-pig-IgG conjugated to Alexa Fluor 488 (all 1:250; Invitrogen). Secondary antibodies were incubated for 1 h at room temperature. Nuclei were labeled with DRAQ5 (1:1000; Cell Signaling Technology). Preparations were mounted in Fluoromount G (Electron Microscopy Services) for imaging.

Zymography

Whole animal *in situ* zymography of wandering third-instars was performed as previously described (Siller and Broadie, 2011). Staged animals were dissected in physiological saline to expose the neuromusculature. Fluorescein-conjugate DQ Gelatin (Molecular Probes, D-12054) was diluted to 500 µg/ml in reaction buffer (50 mM Tris-HCl, 150 mM NaCl, 5 mM $CaCl_2$, 0.2 mM NaN_3, pH 7.6) and applied on preparations for 45 min at 20°C. As a control, 5 mM 1,10-phenanthroline (Molecular Probes) was infused into reaction buffer. Preparations were rinsed with 5× washes in PBS before fixing in 4% paraformaldehyde in PBS for 30 min. Under light agitation, preparations were again washed in PBS for 45 min, then incubated in goat anti-HRP conjugated to Cy3 (1:200; Jackson Laboratories, 123-165-021) for 1 h. Preparations were washed in PBS for 45 min, then mounted in Fluoromount G (Electron Microscopy Services) for imaging. Gelatinase activity was quantified based on the fluorescent signal produced by cleaved DQ Gelatin, as described below (microscopy section).

FM labeling

FM1-43 dye labeling of wandering third-instar NMJs was performed as previously described (Vijayakrishnan et al., 2009). Staged animals were dissected in Ca^{2+}-free physiological saline, and nerves emanating from the VNC were severed. To stimulate SV loading, preparations were incubated for 5 min at 20°C in physiological saline containing 4 µM FM1-43 dye (Molecular Probes), 1.0 mM Ca^{2+} and 90 mM KCl to depolarize motor terminals. Immediately after incubation, preparations were washed 10× with Ca^{2+}-free saline to halt activity during imaging. For unloading, preparations were incubated for 3 min in depolarizing saline (1.0 mM Ca^{2+}, 90 mM KCl) lacking dye. After 10× washes in Ca^{2+}-free saline, the same NMJ terminals were re-imaged. Fluorescence intensity was quantified as described below.

Microscopy analyses

Images were acquired on a Zeiss LSM 510 META laser-scanning confocal microscope. A 63× Plan Apo oil-immersion objective lens was used for all immunocytochemistry, and a 40× water-immersion objective lens was used for all live imaging. *z*-stack images were captured with identical microscope settings for each experiment and analyzed as maximum-intensity projections with ImageJ software (NIH). Fluorescence was quantified as the average pixel intensity within the synaptic area delineated by anti-HRP labeling for all NMJ images, with the exception of live imaging, when FM1-43 dye fluorescence was used. Fluorescence measurements were corrected for background fluorescence and normalized to relative fluorescence units. All imaged NMJs were located on muscle 4 in abdominal segments 3 and 4. For morphological analysis, type Ib synaptic boutons were defined as HRP- and DLG-positive varicosities with a minimum diameter ≥2 µm.

Behavioral assays

Peristaltic muscle contraction was quantified as an indicator of NMJ function as reported previously (Gjorgjieva et al., 2013). Individual wandering third-instars were placed onto the center of an evenly illuminated moist 2% agarose plate and allowed to acclimate for 30 s. Peristaltic waves were video recorded using an Olympus dissection microscope with a mounted Canon Rebel DLSR camera; 1 min of uninterrupted movement was recorded per animal. Videos were analyzed at reduced playback speeds. Peristaltic latencies were quantified as the muscle contraction time from tail to head segments, until the propagation wave was no longer detectable. Six to ten complete peristalses were measured per animal. Automated video tracking was used to quantify movement parameters of freely moving wandering third-instars, including velocity and distance traveled. Ten larvae were placed in the center of 135 mm dishes containing moist 2% agarose, and recorded for 10 min. Videos were imported to ImageJ, binarized by thresholding, and then processed with the TrackMate plugin (Tinevez et al., 2017). Consistent settings were used and validated by manual tracking. Movement tracks were manually assigned to single larva identities. Each track was quantified for distance and time, to calculate average velocity.

Minocycline trials

Minocycline hydrochloride (Sigma-Aldrich) was solubilized in double-distilled H_2O to produce a stock solution, which was then diluted to specified concentrations in the food. Animals were reared from hatching on minocycline diluted in a yeast paste, applied as a thick coating on agar plates. The vehicle controls had an equal volume of double-distilled H_2O added under identical rearing conditions. Both w^{1118} control and $timp^{S1}$ null mutant animals were reared on the plates from hatching until the wandering third-instar stage. Scaled-up experiments for the BMP pMAD signaling pathway were performed by infusing standard cornmeal and molasses food vials with minocycline or vehicle, for side-by-side trials.

Statistics

All data analyses were performed using Microsoft Excel and R version 3.2.5 software. Boxplots display the 25th–75th quartiles as the box with the median denoted as a line and mean as an ×. Boxplot whiskers extend to the minimum and maximum values, excluding outlier points shown as points with values above 1.5 times the interquartile range. Fluorescence measurements had background subtracted and were normalized to controls. Normality assumptions were checked using Shapiro–Wilks tests. All comparisons between two groups were performed by using the two-tailed Welch's unequal variances *t*-test. All comparisons between ≥3 groups were performed by using one-way ANOVA tests, followed by the Tukey-Kramer pairwise post-hoc test. Data are reported in the text as mean±s.e.m.

Acknowledgements

We thank Peter ten Dijke (Leiden University, The Netherlands) for the gift of pMAD antibody. We are grateful to the Bloomington *Drosophila* Stock Center (BDSC; Bloomington, IN, USA), Vienna *Drosophila* Resource Center (VDRC; Vienna, Austria) and Developmental Studies Hybridoma Bank (DSHB; University of Iowa, Iowa City, IA, USA) for providing essential genetic lines and antibodies, respectively.

Competing interests

The authors declare no competing or financial interests.

Author contributions

Conceptualization: J.S., K.B.; Methodology: J.S., K.B.; Software: J.S.; Validation: J.S.; Formal analysis: J.S.; Investigation: J.S.; Resources: K.B.; Writing - original draft: J.S.; Writing - review & editing: J.S., K.B.; Visualization: J.S., K.B.; Supervision: K.B.; Project administration: K.B.; Funding acquisition: J.S., K.B.

Funding

This work was supported by National Institutes of Health (MH096832 to K.B.). J.S. was supported by the Searle Systems Biology & Bioengineering Undergraduate Research program and LittleJohn Fellowship for undergraduate research at Vanderbilt University. Deposited in PMC for release after 12 months.

Supplementary information

Supplementary information available online at
http://jcs.biologists.org/lookup/doi/10.1242/jcs.200808.supplemental

References

Abdallah, M. W. and Michel, T. M. (2013). Matrix metalloproteinases in autism spectrum disorders. *J. Mol. Psychiatry* **1**, 16.

Arpino, V., Brock, M. and Gill, S. E. (2015). The role of TIMPs in regulation of extracellular matrix proteolysis. *Matrix Biol.* **44-46**, 247-254.

Ball, R. W., Warren-Paquin, M., Tsurudome, K., Liao, E. H., Elazzouzi, F., Cavanagh, C., An, B.-S., Wang, T.-T., White, J. H. and Haghighi, A. P. (2010). Retrograde BMP signaling controls synaptic growth at the NMJ by regulating trio expression in motor neurons. *Neuron* **66**, 536-549.

Berke, B., Wittnam, J., McNeill, E., Van Vactor, D. L. and Keshishian, H. (2013). Retrograde BMP signaling at the synapse: a permissive signal for synapse maturation and activity-dependent plasticity. *J. Neurosci.* **33**, 17937-17950.

Berni, J., Pulver, S. R., Griffith, L. C. and Bate, M. (2012). Autonomous circuitry for substrate exploration in freely moving Drosophila larvae. *Curr. Biol.* **22**, 1861-1870.

Betz, W. J. and Bewick, G. S. (1992). Optical analysis of synaptic vesicle recycling at the frog neuromuscular junction. *Science* **255**, 200-203.

Bilousova, T. V., Dansie, L., Ngo, M., Aye, J., Charles, J. R., Ethell, D. W. and Ethell, I. M. (2009). Minocycline promotes dendritic spine maturation and improves behavioural performance in the fragile X mouse model. *J. Med. Genet.* **46**, 94-102.

Bour, B. A., O'Brien, M. A., Lockwood, W. L., Goldstein, E. S., Bodmer, R., Taghert, P. H., Abmayr, S. M. and Nguyen, H. T. (1995). Drosophila MEF2, a transcription factor that is essential for myogenesis. *Genes Dev.* **9**, 730-741.

Brkic, M., Balusu, S., Libert, C. and Vandenbroucke, R. E. (2015). Friends or foes: matrix metalloproteinases and their multifaceted roles in neurodegenerative diseases. *Mediators Inflamm.* **2015**, 620581.

Broadie, K., Baumgartner, S. and Prokop, A. (2011). Extracellular matrix and its receptors in Drosophila neural development. *Dev. Neurobiol.* **71**, 1102-1130.

Collins, C. A. and DiAntonio, A. (2007). Synaptic development: insights from Drosophila. *Curr. Opin. Neurobiol.* **17**, 35-42.

Crocker, S. J., Pagenstecher, A. and Campbell, I. L. (2004). The TIMPs tango with MMPs and more in the central nervous system. *J. Neurosci. Res.* **75**, 1-11.

Dani, N. and Broadie, K. (2012). Glycosylated synaptomatrix regulation of trans-synaptic signaling. *Dev. Neurobiol.* **72**, 2-21.

Dani, N., Nahm, M., Lee, S. and Broadie, K. (2012). A targeted glycan-related gene screen reveals heparan sulfate proteoglycan sulfation regulates WNT and BMP trans-synaptic signaling. *PLoS Genet.* **8**, e1003031.

Dani, N., Zhu, H. and Broadie, K. (2014). Two protein N-acetylgalactosaminyl transferases regulate synaptic plasticity by activity-dependent regulation of integrin signaling. *J. Neurosci.* **34**, 13047-13065.

Dansie, L. E. and Ethell, I. M. (2011). Casting a net on dendritic spines: the extracellular matrix and its receptors. *Dev. Neurobiol.* **71**, 956-981.

Dansie, L. E., Phommahaxay, K., Okusanya, A. G., Uwadia, J., Huang, M., Rotschafer, S. E., Razak, K. A., Ethell, D. W. and Ethell, I. M. (2013). Long-lasting effects of minocycline on behavior in young but not adult Fragile X mice. *Neuroscience* **246**, 186-198.

Dear, M. L., Dani, N., Parkinson, W., Zhou, S. and Broadie, K. (2016). Two classes of matrix metalloproteinases reciprocally regulate synaptogenesis. *Development* **143**, 75-87.

Diaper, D. C., Adachi, Y., Sutcliffe, B., Humphrey, D. M., Elliott, C. J. H., Stepto, A., Ludlow, Z. N., Vanden Broeck, L., Callaerts, P., Dermaut, B. et al. (2013). Loss and gain of Drosophila TDP-43 impair synaptic efficacy and motor control leading to age-related neurodegeneration by loss-of-function phenotypes. *Hum. Mol. Genet.* **22**, 1539-1557.

Dietzl, G., Chen, D., Schnorrer, F., Su, K.-C., Barinova, Y., Fellner, M., Gasser, B., Kinsey, K., Oppel, S., Scheiblauer, S. et al. (2007). A genome-wide transgenic RNAi library for conditional gene inactivation in Drosophila. *Nature* **448**, 151-156.

Dityatev, A. and Schachner, M. (2003). Extracellular matrix molecules and synaptic plasticity. *Nat. Rev. Neurosci.* **4**, 456-468.

Dityatev, A., Schachner, M. and Sonderegger, P. (2010). The dual role of the extracellular matrix in synaptic plasticity and homeostasis. *Nat. Rev. Neurosci.* **11**, 735-746.

Doll, C. A. and Broadie, K. (2014). Impaired activity-dependent neural circuit assembly and refinement in autism spectrum disorder genetic models. *Front. Cell. Neurosci.* **8**, 30.

Dziembowska, M. and Wlodarczyk, J. (2012). MMP9: a novel function in synaptic plasticity. *Int. J. Biochem. Cell Biol.* **44**, 709-713.

Dziembowska, M., Pretto, D. I., Janusz, A., Kaczmarek, L., Leigh, M. J., Gabriel, N., Durbin-Johnson, B., Hagerman, R. J. and Tassone, F. (2013). High MMP-9 activity levels in fragile X syndrome are lowered by minocycline. *Am. J. Med. Genet. A.* **161**, 1897-1903.

Friedman, S. H., Dani, N., Rushton, E. and Broadie, K. (2013). Fragile X mental retardation protein regulates trans-synaptic signaling in Drosophila. *Dis. Model. Mech.* **6**, 1400-1413.

Gaffield, M. A. and Betz, W. J. (2007). Imaging synaptic vesicle exocytosis and endocytosis with FM dyes. *Nat. Protoc.* **1**, 2916-2921.

Gjorgjieva, J., Berni, J., Evers, J. F. and Eglen, S. J. (2013). Neural circuits for peristaltic wave propagation in crawling Drosophila larvae: analysis and modeling. *Front. Comput. Neurosci.* **7**, 24.

Godenschwege, T. A., Pohar, N., Buchner, S. and Buchner, E. (2000). Inflated wings, tissue autolysis and early death in tissue inhibitor of metalloproteinases mutants of Drosophila. *Eur. J. Cell Biol.* **79**, 495-501.

Godenschwege, T. A., Reisch, D., Diegelmann, S., Eberle, K., Funk, N., Heisenberg, M., Hoppe, V., Hoppe, J., Klagges, B. R. E., Martin, J.-R. et al. (2004). Flies lacking all synapsins are unexpectedly healthy but are impaired in complex behaviour. *Eur. J. Neurosci.* **20**, 611-622.

Golub, L. M., Ramamurthy, N. S., McNamara, T. F., Greenwald, R. A. and Rifkin, B. R. (1991). Tetracyclines inhibit connective tissue breakdown: new therapeutic implications for an old family of drugs. *Crit. Rev. Oral Biol. Med.* **2**, 297-321.

Gratz, S. J., Cummings, A. M., Nguyen, J. N., Hamm, D. C., Donohue, L. K., Harrison, M. M., Wildonger, J. and O'Connor-Giles, K. M. (2013). Genome engineering of Drosophila with the CRISPR RNA-guided Cas9 nuclease. *Genetics* **194**, 1029-1035.

Hadler-Olsen, E., Fadnes, B., Sylte, I., Uhlin-Hansen, L. and Winberg, J.-O. (2011). Regulation of matrix metalloproteinase activity in health and disease. *FEBS J.* **278**, 28-45.

Heikkinen, A., Pihlajaniemi, T., Faissner, A. and Yuzaki, M. (2014). Neural ECM and synaptogenesis. *Prog. Brain Res.* **214**, 29-51.

Huntley, G. W. (2012). Synaptic circuit remodelling by matrix metalloproteinases in health and disease. *Nat. Rev. Neurosci.* **13**, 743-757.

James, R. E. and Broihier, H. T. (2011). Crimpy inhibits the BMP homolog Gbb in motoneurons to enable proper growth control at the Drosophila neuromuscular junction. *Development* **138**, 3273-3286.

James, R. E., Hoover, K. M., Bulgari, D., McLaughlin, C. N., Wilson, C. G., Wharton, K. A., Levitan, E. S. and Broihier, H. T. (2014). Crimpy enables discrimination of presynaptic and postsynaptic pools of a BMP at the Drosophila neuromuscular junction. *Dev. Cell* **31**, 586-598.

Jaworski, D. M., Soloway, P., Caterina, J. and Falls, W. A. (2006). Tissue inhibitor of metalloproteinase-2 (TIMP-2)-deficient mice display motor deficits. *J. Neurobiol.* **66**, 82-94.

Jaworski, D. M., Beem-Miller, M., Lluri, G. and Barrantes-Reynolds, R. (2007). Potential regulatory relationship between the nested gene DDC8 and its host gene tissue inhibitor of metalloproteinase-2. *Physiol. Genomics* **28**, 168-178.

Jumbo-Lucioni, P. P., Parkinson, W. M., Kopke, D. L. and Broadie, K. (2016). Coordinated movement, neuromuscular synaptogenesis and trans-synaptic signaling defects in Drosophila galactosemia models. *Hum. Mol. Genet.* **25**, 3699-3714.

Kashima, R., Roy, S., Ascano, M., Martinez-Cerdeno, V., Ariza-Torres, J., Kim, S., Louie, J., Lu, Y., Leyton, P., Bloch, K. D. et al. (2016). Augmented noncanonical BMP type II receptor signaling mediates the synaptic abnormality of fragile X syndrome. *Sci. Signal.* **9**, ra58.

Keshishian, H. and Kim, Y.-S. (2004). Orchestrating development and function: retrograde BMP signaling in the Drosophila nervous system. *Trends Neurosci.* **27**, 143-147.

Kessenbrock, K., Plaks, V. and Werb, Z. (2010). Matrix metalloproteinases: regulators of the tumor microenvironment. *Cell* **141**, 52-67.

Kim, N. C. and Marqués, G. (2012). The Ly6 neurotoxin-like molecule target of wit regulates spontaneous neurotransmitter release at the developing neuromuscular junction in Drosophila. *Dev. Neurobiol.* **72**, 1541-1558.

Kurshan, P. T., Phan, A. Q., Wang, G. J., Crane, M. M., Lu, H. and Shen, K. (2014). Regulation of synaptic extracellular matrix composition is critical for proper synapse morphology. *J. Neurosci.* **34**, 12678-12689.

Larraín, J., Bachiller, D., Lu, B., Agius, E., Piccolo, S. and De Robertis, E. M. (2000). BMP-binding modules in chordin: a model for signalling regulation in the extracellular space. *Development* **127**, 821-830.

Larraín, J., Oelgeschläger, M., Ketpura, N. I., Reversade, B., Zakin, L. and De Robertis, E. M. (2001). Proteolytic cleavage of Chordin as a switch for the dual activities of Twisted gastrulation in BMP signaling. *Development* **128**, 4439-4447.

Journal of Cell Science

Lee, Y. C. G. and Chang, H.-H. (2013). The evolution and functional significance of nested gene structures in Drosophila melanogaster. *Genome Biol. Evol.* **5**, 1978-1985.
Leigh, M. J. S., Nguyen, D. V., Mu, Y., Winarni, T. I., Schneider, A., Chechi, T., Polussa, J., Doucet, P., Tassone, F., Rivera, S. M. et al. (2013). A randomized double-blind, placebo-controlled trial of minocycline in children and adolescents with fragile x syndrome. *J. Dev. Behav. Pediatr.* **34**, 147-155.
Lepeta, K. and Kaczmarek, L. (2015). Matrix metalloproteinase-9 as a novel player in synaptic plasticity and schizophrenia. *Schizophr. Bull.* **41**, 1003-1009.
Liu, W.-T., Han, Y., Liu, Y.-P., Song, A. A., Barnes, B. and Song, X.-J. (2010). Spinal matrix metalloproteinase-9 contributes to physical dependence on morphine in mice. *J. Neurosci.* **30**, 7613-7623.
Llano, E., Pendás, A. M., Aza-Blanc, P., Kornberg, T. B. and López-Otín, C. (2000). Dm1-MMP, a matrix metalloproteinase from Drosophila with a potential role in extracellular matrix remodeling during neural development. *J. Biol. Chem.* **275**, 35978-35985.
Lluri, G., Langlois, G. D., McClellan, B., Soloway, P. D. and Jaworski, D. M. (2006). Tissue inhibitor of metalloproteinase-2 (TIMP-2) regulates neuromuscular junction development via a beta1 integrin-mediated mechanism. *J. Neurobiol.* **66**, 1365-1377.
Luo, L., Liao, Y. J., Jan, L. Y. and Jan, Y. N. (1994). Distinct morphogenetic functions of similar small GTPases: Drosophila Drac1 is involved in axonal outgrowth and myoblast fusion. *Genes Dev.* **8**, 1787-1802.
Magnowska, M., Gorkiewicz, T., Suska, A., Wawrzyniak, M., Rutkowska-Wlodarczyk, I., Kaczmarek, L. and Wlodarczyk, J. (2016). Transient ECM protease activity promotes synaptic plasticity. *Sci. Rep.* **6**, 27757.
Malemud, C. J. (2006). Matrix metalloproteinases (MMPs) in health and disease: an overview. *Front. Biosci. J. Virtual Libr.* **11**, 1696-1701.
Marqués, G. and Zhang, B. (2006). Retrograde signaling that regulates synaptic development and function at the Drosophila neuromuscular junction. *Int. Rev. Neurobiol.* **75**, 267-285.
McCabe, B. D., Marqués, G., Haghighi, A. P., Fetter, R. D., Crotty, M. L., Haerry, T. E., Goodman, C. S. and O'Connor, M. B. (2003). The BMP homolog Gbb provides a retrograde signal that regulates synaptic growth at the Drosophila neuromuscular junction. *Neuron* **39**, 241-254.
Menon, K. P., Carrillo, R. A. and Zinn, K. (2013). Development and plasticity of the Drosophila larval neuromuscular junction. *Wiley Interdiscip. Rev. Dev. Biol.* **2**, 647-670.
Michels, B., Diegelmann, S., Tanimoto, H., Schwenkert, I., Buchner, E. and Gerber, B. (2005). A role for Synapsin in associative learning: the Drosophila larva as a study case. *Learn. Mem.* **12**, 224-231.
Miller, C. M., Page-McCaw, A. and Broihier, H. T. (2008). Matrix metalloproteinases promote motor axon fasciculation in the Drosophila embryo. *Development* **135**, 95-109.
Miller, C. M., Liu, N., Page-McCaw, A. and Broihier, H. T. (2011). Drosophila Mmp2 regulates the matrix molecule Faulty attraction (Frac) to promote motor axon targeting in Drosophila. *J. Neurosci.* **31**, 5335-5347.
Miller, D. L., Ballard, S. L. and Ganetzky, B. (2012). Analysis of synaptic growth and function in Drosophila with an extended larval stage. *J. Neurosci.* **32**, 13776-13786.
Mittal, R., Patel, A. P., Debs, L. H., Nguyen, D., Patel, K., Grati, M., Mittal, J., Yan, D., Chapagain, P. and Liu, X. Z. (2016). Intricate functions of matrix metalloproteinases in physiological and pathological conditions. *J. Cell. Physiol.* **231**, 2599-2621.
Moore, C. S. and Crocker, S. J. (2012). An alternate perspective on the roles of TIMPs and MMPs in pathology. *Am. J. Pathol.* **180**, 12-16.
Nahm, M., Long, A. A., Paik, S. K., Kim, S., Bae, Y. C., Broadie, K. and Lee, S. (2010). The Cdc42-selective GAP Rich regulates postsynaptic development and retrograde BMP transsynaptic signaling. *J. Cell Biol.* **191**, 661-675.
Nahm, M., Lee, M.-J., Parkinson, W., Lee, M., Kim, H., Kim, Y.-J., Kim, S., Cho, Y. S., Min, B.-M., Bae, Y. C. et al. (2013). Spartin regulates synaptic growth and neuronal survival by inhibiting BMP-mediated microtubule stabilization. *Neuron* **77**, 680-695.
Ould-yahoui, A., Tremblay, E., Sbai, O., Ferhat, L., Bernard, A., Charrat, E., Gueye, Y., Lim, N. H., Brew, K., Risso, J.-J. et al. (2009). A new role for TIMP-1 in modulating neurite outgrowth and morphology of cortical neurons. *PLoS ONE* **4**, e8289.
Page-McCaw, A., Serano, J., Santé, J. M. and Rubin, G. M. (2003). Drosophila matrix metalloproteinases are required for tissue remodeling, but not embryonic development. *Dev. Cell* **4**, 95-106.
Page-McCaw, A., Ewald, A. J. and Werb, Z. (2007). Matrix metalloproteinases and the regulation of tissue remodelling. *Nat. Rev. Mol. Cell Biol.* **8**, 221-233.
Parkinson, W. M., Dookwah, M., Dear, M. L., Gatto, C. L., Aoki, K., Tiemeyer, M. and Broadie, K. (2016). Synaptic roles for phosphomannomutase type 2 in a new Drosophila congenital disorder of glycosylation disease model. *Dis. Model. Mech.* **9**, 513-527.
Persson, U., Izumi, H., Souchelnytskyi, S., Itoh, S., Grimsby, S., Engström, U., Heldin, C.-H., Funa, K. and ten Dijke, P. (1998). The L45 loop in type I receptors for TGF-beta family members is a critical determinant in specifying Smad isoform activation. *FEBS Lett.* **434**, 83-87.
Piccioli, Z. D. and Littleton, J. T. (2014). Retrograde BMP signaling modulates rapid activity-dependent synaptic growth via presynaptic LIM kinase regulation of cofilin. *J. Neurosci.* **34**, 4371-4381.
Pohar, N., Godenschwege, T. A. and Buchner, E. (1999). Invertebrate tissue inhibitor of metalloproteinase: structure and nested gene organization within the synapsin locus is conserved from Drosophila to human. *Genomics* **57**, 293-296.
Pollock, E., Everest, M., Brown, A. and Poulter, M. O. (2014). Metalloproteinase inhibition prevents inhibitory synapse reorganization and seizure genesis. *Neurobiol. Dis.* **70**, 21-31.
Port, F., Chen, H.-M., Lee, T. and Bullock, S. L. (2014). Optimized CRISPR/Cas tools for efficient germline and somatic genome engineering in Drosophila. *Proc. Natl. Acad. Sci. USA* **111**, E2967-E2976.
Pulver, S. R., Pashkovski, S. L., Hornstein, N. J., Garrity, P. A. and Griffith, L. C. (2009). Temporal dynamics of neuronal activation by Channelrhodopsin-2 and TRPA1 determine behavioral output in *Drosophila* larvae. *J. Neurophysiol.* **101**, 3075-3088.
Pulver, S. R., Bayley, T. G., Taylor, A. L., Berni, J., Bate, M. and Hedwig, B. (2015). Imaging fictive locomotor patterns in larval. *Drosophila. J. Neurophysiol.* **114**, 2564-2577.
Reinhard, S. M., Razak, K. and Ethell, I. M. (2015). A delicate balance: role of MMP-9 in brain development and pathophysiology of neurodevelopmental disorders. *Front. Cell. Neurosci.* **9**, 280.
Renger, J. J., Ueda, A., Atwood, H. L., Govind, C. K. and Wu, C. F. (2000). Role of cAMP cascade in synaptic stability and plasticity: ultrastructural and physiological analyses of individual synaptic boutons in Drosophila memory mutants. *J. Neurosci.* **20**, 3980-3992.
Rivera, S., Khrestchatisky, M., Kaczmarek, L., Rosenberg, G. A. and Jaworski, D. M. (2010). Metzincin proteases and their inhibitors: foes or friends in nervous system physiology? *J. Neurosci.* **30**, 15337-15357.
Schleede, J. and Blair, S. S. (2015). The Gyc76C receptor guanylyl cyclase and the Foraging cGMP-dependent kinase regulate extracellular matrix organization and BMP signaling in the developing wing of Drosophila melanogaster. *PLoS Genet.* **11**, e1005576.
Sengle, G., Charbonneau, N. L., Ono, R. N., Sasaki, T., Alvarez, J., Keene, D. R., Bächinger, H. P. and Sakai, L. Y. (2008). Targeting of bone morphogenetic protein growth factor complexes to fibrillin. *J. Biol. Chem.* **283**, 13874-13888.
Sidhu, H., Dansie, L. E., Hickmott, P. W., Ethell, D. W. and Ethell, I. M. (2014). Genetic removal of matrix metalloproteinase 9 rescues the symptoms of fragile X syndrome in a mouse model. *J. Neurosci.* **34**, 9867-9879.
Siller, S. S. and Broadie, K. (2011). Neural circuit architecture defects in a Drosophila model of Fragile X syndrome are alleviated by minocycline treatment and genetic removal of matrix metalloproteinase. *Dis. Model. Mech.* **4**, 673-685.
Siller, S. S. and Broadie, K. (2012). Matrix metalloproteinases and minocycline: therapeutic avenues for fragile X syndrome. *Neural Plast.* **2012**, 124548.
Smith, R. B., Machamer, J. B., Kim, N. C., Hays, T. S. and Marqués, G. (2012). Relay of retrograde synaptogenic signals through axonal transport of BMP receptors. *J. Cell Sci.* **125**, 3752-3764.
Staples, J. and Broadie, K. (2013). The cell polarity scaffold Lethal Giant Larvae regulates synapse morphology and function. *J. Cell Sci.* **126**, 1992-2003.
Stetler-Stevenson, W. G. (2008). Tissue inhibitors of metalloproteinases in cell signaling: metalloproteinase-independent biological activities. *Sci. Signal.* **1**, re6.
Sulkowski, M., Kim, Y.-J. and Serpe, M. (2014). Postsynaptic glutamate receptors regulate local BMP signaling at the Drosophila neuromuscular junction. *Development* **141**, 436-447.
Sulkowski, M. J., Han, T. H., Ott, C., Wang, Q., Verheyen, E. M., Lippincott-Schwartz, J. and Serpe, M. (2016). A novel, noncanonical BMP pathway modulates synapse maturation at the Drosophila neuromuscular junction. *PLoS Genet.* **12**, e1005810.
Szklarczyk, A., Conant, K., Owens, D. F., Ravin, R., McKay, R. D. and Gerfen, C. (2007). Matrix metalloproteinase-7 modulates synaptic vesicle recycling and induces atrophy of neuronal synapses. *Neuroscience* **149**, 87-98.
Tinevez, J.-Y., Perry, N., Schindelin, J., Hoopes, G. M., Reynolds, G. D., Laplantine, E., Bednarek, S. Y., Shorte, S. L. and Eliceiri, K. W. (2017). TrackMate: an open and extensible platform for single-particle tracking. *Methods* **115**, 80-90.
Tsilibary, E., Tzinia, A., Radenovic, L., Stamenkovic, V., Lebitko, T., Mucha, M., Pawlak, R., Frischknecht, R. and Kaczmarek, L. (2014). Neural ECM proteases in learning and synaptic plasticity. *Prog. Brain Res.* **214**, 135-157.
Ueda, A., Grabbe, C., Lee, J., Lee, J., Palmer, R. H. and Wu, C.-F. (2008). Mutation of Drosophila focal adhesion kinase induces bang-sensitive behavior and disrupts glial function, axonal conduction and synaptic transmission. *Eur. J. Neurosci.* **27**, 2860-2870.
VanSaun, M., Herrera, A. A. and Werle, M. J. (2003). Structural alterations at the neuromuscular junctions of matrix metalloproteinase 3 null mutant mice. *J. Neurocytol.* **32**, 1129-1142.
Vasin, A., Zueva, L., Torrez, C., Volfson, D., Littleton, J. T. and Bykhovskaia, M. (2014). Synapsin regulates activity-dependent outgrowth of synaptic boutons at the Drosophila neuromuscular junction. *J. Neurosci.* **34**, 10554-10563.

Vijayakrishnan, N., Woodruff, E. A. and Broadie, K. (2009). Rolling blackout is required for bulk endocytosis in non-neuronal cells and neuronal synapses. *J. Cell Sci.* **122**, 114-125.
Wang, H., Russa, M. L. and Qi, L. S. (2016). CRISPR/Cas9 in genome editing and beyond. *Annu. Rev. Biochem.* **85**, 227-264.
Wei, S., Xie, Z., Filenova, E. and Brew, K. (2003). Drosophila TIMP is a potent inhibitor of MMPs and TACE: similarities in structure and function to TIMP-3. *Biochemistry* **42**, 12200-12207.
Wharton, K. A., Cook, J. M., Torres-Schumann, S., de Castro, K., Borod, E. and Phillips, D. A. (1999). Genetic analysis of the bone morphogenetic protein-related gene, gbb, identifies multiple requirements during Drosophila development. *Genetics* **152**, 629-640.
Wu, H., Xiong, W. C. and Mei, L. (2010). To build a synapse: signaling pathways in neuromuscular junction assembly. *Development* **137**, 1017-1033.
Yamamoto, K., Murphy, G. and Troeberg, L. (2015). Extracellular regulation of metalloproteinases. *Matrix Biol.* **44-46**, 255-263.
Yasunaga, K.-I., Kanamori, T., Morikawa, R., Suzuki, E. and Emoto, K. (2010). Dendrite reshaping of adult Drosophila sensory neurons requires matrix metalloproteinase-mediated modification of the basement membranes. *Dev. Cell* **18**, 621-632.
Zhai, Z., Ha, N., Papagiannouli, F., Hamacher-Brady, A., Brady, N., Sorge, S., Bezdan, D. and Lohmann, I. (2012). Antagonistic regulation of apoptosis and differentiation by the Cut transcription factor represents a tumor-suppressing mechanism in Drosophila. *PLoS Genet.* **8**, e1002582.
Zhang, Y. Q., Bailey, A. M., Matthies, H. J. G., Renden, R. B., Smith, M. A., Speese, S. D., Rubin, G. M. and Broadie, K. (2001). Drosophila fragile X-related gene regulates the MAP1B homolog futsch to control synaptic structure and function. *Cell* **107**, 591-603.
Zhao, G., Wu, Y., Du, L., Li, W., Xiong, Y., Yao, A., Wang, Q. and Zhang, Y. Q. (2015). Drosophila S6 Kinase like inhibits neuromuscular junction growth by downregulating the BMP receptor thickveins. *PLoS Genet.* **11**, e1004984.